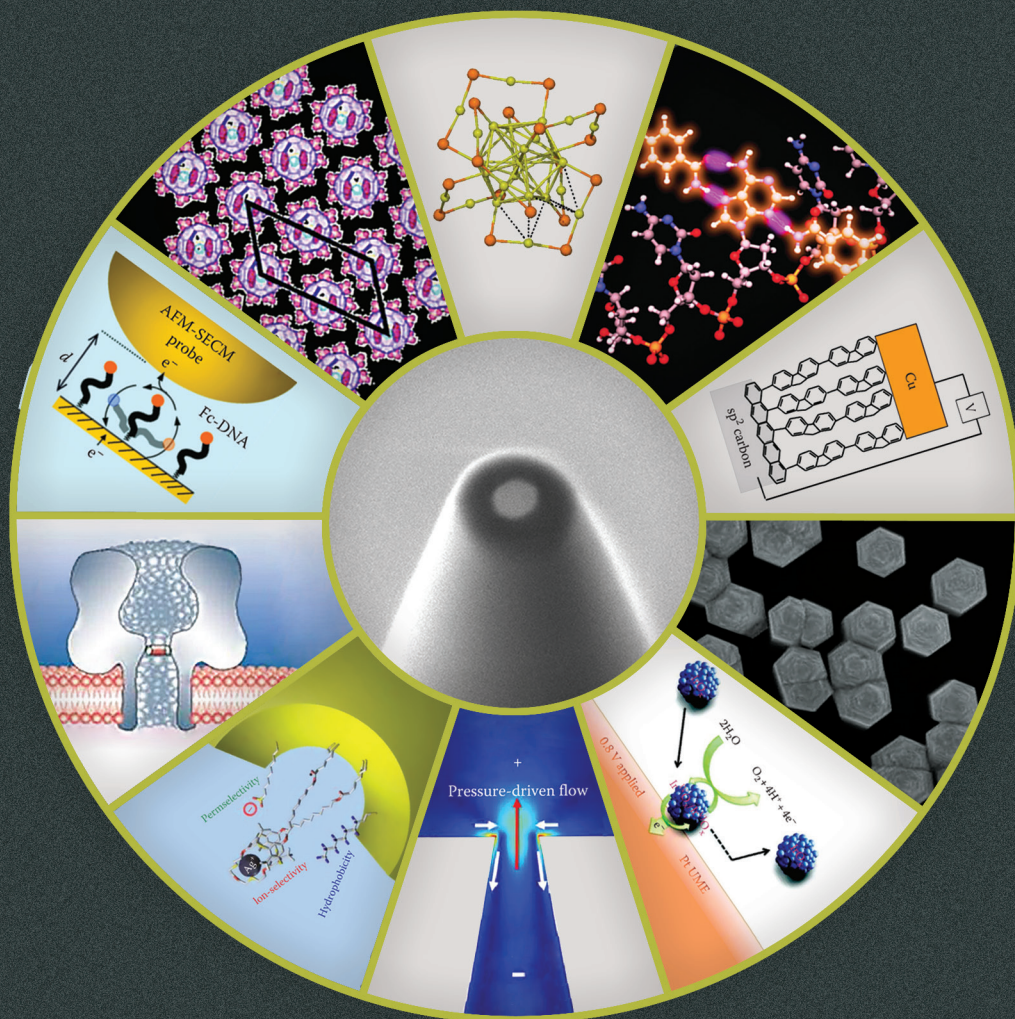


NANOELECTROCHEMISTRY



edited by
Michael V. Mirkin • Shigeru Amemiya



CRC Press
Taylor & Francis Group

15 Nanoelectrodes and Liquid/ Liquid Nanointerfaces

Michael V. Mirkin

CONTENTS

15.1	Introduction	540
15.2	Fabrication and Characterization of Metal Nanoelectrodes	540
15.2.1	Fabrication and Basic Features of Nanoelectrodes with Different Geometries	540
15.2.1.1	Nanoband Electrodes	540
15.2.1.2	Conical Nanoelectrodes	541
15.2.1.3	Spherical-Cap Electrodes	541
15.2.1.4	Inlaid Disk	542
15.2.1.5	Recessed Disk and Nanopore	543
15.2.2	Characterization of Nanoelectrodes: Voltammetry and SECM	543
15.2.3	Characterization of Nanoelectrodes: Electron Microscopy and AFM.....	545
15.3	Nanopipette-Supported ITIES.....	549
15.3.1	Electrochemistry at Nano-ITIES.....	549
15.3.2	Fabrication and Characterization of Nanopipettes	549
15.3.2.1	Pulling a Nanopipette	549
15.3.2.2	Surface Modification.....	550
15.3.2.3	Characterization of Nanopipettes	550
15.3.3	Electrochemical Measurements at Nanopipettes.....	553
15.4	Kinetics of Charge-Transfer Reactions at the Nanointerfaces.....	554
15.4.1	Mass-Transfer and Kinetic Measurements at Nanointerfaces	554
15.4.2	Kinetics of Electron-Transfer Reactions at the Nanoelectrodes	556
15.4.3	Kinetics of Charge-Transfer Reactions at the Nano-ITIES.....	557
15.4.3.1	Electron-Transfer Kinetics	557
15.4.3.2	Ion-Transfer Kinetics	558
15.4.3.3	Some Experimental Issues	559
15.4.4	Common Ion Voltammetry	561
15.5	Special Nanoelectrochemical Probes	563
15.5.1	Nano-TLC	563
15.5.2	Carbon-Based Nanoelectrodes and Pipettes.....	564
15.5.3	Dual Nanoelectrodes and Pipettes.....	565
15.5.4	Electrochemical Attosyringe	567
15.6	Summary and Outlook	567
	Acknowledgments.....	567
	References.....	567

15.1 INTRODUCTION

To perform electrochemical experiments on the nanoscale and probe nanometer-sized objects, one needs comparably sized electrochemical tools.¹ A number of such tools—solid nanoelectrodes and nanopipette-supported liquid/liquid interfaces—have been developed since the late 1980s.^{2,3} This review is concerned with new challenges and opportunities stemming from the use of nanoelectrochemical approaches. While nanoprobe offers important advantages and allow one to study numerous phenomena that cannot be observed at macroscopic electrodes, the visualization of their surfaces remains challenging, and the interpretation of the electrochemical response relies on assumptions about the electrode size and geometry. Here, we discuss methodologies that have been used to fabricate and characterize electrochemical nanoprobe and some typical pitfalls encountered in nanoelectrochemical experiments.

A wide variety of nanoelectrode shapes and features have recently been reported. In this chapter, we will only discuss several representative geometries as well as general concepts and approaches to nanoelectrochemical experiments. The survey of other geometries (such as a nanoring or a cylindrically shaped nanotube/nanowire) as well as arrays of nanoelectrodes can be found in recent review articles.^{1,4} The nanoelectrode theory is not discussed here. As long as a nanoelectrode is not too small, its behavior follows classical microelectrode theory; and the theoretical description of nanosize-related effects on electrochemical processes is reviewed in Chapters 1 and 2. The applications of nanoelectrodes and nanopipettes range from the studies of biological and artificial membranes⁵ to single-nanoparticle electrocatalysis⁶ to nucleation/growth of metals.⁷ To avoid overlap with other chapters, the review of applications is limited to studies of charge-transfer (CT) reactions, and the works employing nanoelectrodes/pipettes as scanning electrochemical microscope (SECM) and scanning electrochemical cell microscopy (SECCM) tips will be surveyed in Chapters 18 and 19.

15.2 FABRICATION AND CHARACTERIZATION OF METAL NANO-ELECTRODES

The fabrication of a nanoelectrode can be deceptively easy: by using a laser pipette puller, it takes only a few minutes to seal a commercially available metal wire into glass and obtain an electrode with an effective radius on the nanometer scale. However, most of those electrodes are likely to be unsuitable for quantitative measurements. In this section, we survey methodologies developed for making and characterizing different types of nanoelectrodes as well as some issues affecting the reliability of nanoelectrochemical experiments.

15.2.1 FABRICATION AND BASIC FEATURES OF NANO-ELECTRODES WITH DIFFERENT GEOMETRIES

Several representative nanoelectrode geometries are shown schematically in Figure 15.1. Historically, the first submicrometer-sized electrochemical electrode was a nanoband (Figure 15.1a) produced by the Wightman group.^{2a} Other geometries, including (b) conical electrode, (c) spherical cap, (d) inlaid and (e) recessed disks, and (f) nanopore, have been reported. Nanoelectrodes of different kinds offer specific advantages (and disadvantages) and are suitable for different applications.

15.2.1.1 Nanoband Electrodes

These electrodes can be fabricated by forming a thin film of the electrode material between two insulating layers.² Such a film can be either obtained commercially or produced on an insulating substrate by a sputtering technique and then covered by an insulating overlayer. The edge of this assembly exposed to the solution serves as a voltammetric electrode with a nanoscopic width (e.g., 5–2300 nm^{2a}) and a macroscopic length (mm or cm). The high mass-transfer rate and quasi-steady-state response are due to the nanoscale bandwidth, while the macroscopic length was initially seen

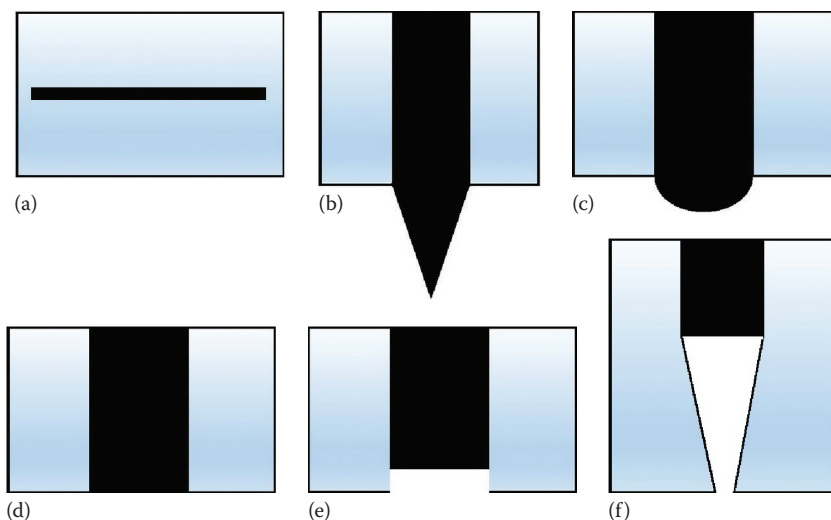


FIGURE 15.1 Examples of nanoelectrode geometries: (a) band, (b) conical electrode, (c) spherical cap, (d) inlaid disk, (e) recessed disk, and (f) nanopore.

as an advantage because of significantly higher Faradaic currents flowing at band electrodes as compared to disks or cones with similar characteristic dimensions (i.e., the radius comparable to the half width of the band). The macroscopic length eventually limited applications of band electrodes, which cannot be used as scanning probes and are not suitable for experiments in small volumes that require small physical size.

15.2.1.2 Conical Nanoelectrodes

The methodology for fabricating conical nanoelectrodes was originally developed to produce scanning tunneling microscope (STM) tips.^{8,9} A micrometer-diameter metal wire (e.g., a 125 μm Pt/Ir rod⁸) was etched electrochemically and insulated with molten Apiezon wax,⁹ glass,¹⁰ polymer,^{10,11} or electrophoretic paint.¹² Similar approaches were used to produce conical carbon nanoelectrodes.¹³ The very end of a conical tip was exposed by placing it in an STM and applying voltage (e.g., 10 V) between the tip and a conductive substrate (e.g., a Pt disk). The onset of current flow produced a hole in the tip insulation at the point of closest approach of the tip to the substrate, while leaving most of the tip still insulated.¹⁴ Other methods, such as heat shrinkage of the coating film,¹² have also been used to expose the tip.

The sharp tip of conical nanoelectrodes rendered them useful for penetrating thin films.^{14b,c} They have also been used for SECM imaging (see Chapter 18). However, they are less useful for quantitative applications because of the intrinsically imperfect shape and nonpolishable surface.

15.2.1.3 Spherical-Cap Electrodes

Quasi-hemispherical and spherical-cap electrodes (Figure 15.1c) produced by etching metal wires or carbon fibers are not very different from conical nanoelectrodes. Because the exact shape characterization is difficult for both types of electrodes, no clear distinction was made between them in several publications.^{10a,12,15}

Spherical-cap electrodes can also be produced by electrodeposition. Three-dimensional nucleation/growth produces metal crystals shaped as a quasi-hemisphere or a spherical cap.¹⁶ The deposit shape is nearly perfect for a liquid metal, for example, Hg. This process was used to produce Hg microelectrodes^{17a} and—more recently—nanoelectrodes.^{17b} Such electrodes are suitable for electroanalysis and can be employed as SECM tips.^{17a,c}

15.2.1.4 Inlaid Disk

The inlaid disk geometry, in which the conductive disk surface is flush with that of the surrounding insulator, is the most popular electrode geometry in general and the hardest to fabricate on the nanoscale. The insulating sheath of such electrodes can be either finite (i.e., the insulator radius, r_g , is comparable to the conductive disk radius, a) or essentially infinite (i.e., $r_g \gg a$). The fabrication procedures are different: the thin-sheath electrodes have been produced by pulling a metal wire into a glass capillary using a micropipette puller,¹⁸ while the first step in the preparation of embedded disks is sealing an electrochemically sharpened metal microwire into a glass capillary without pulling.¹⁹ While thick-glass electrodes are robust and relatively easy to fabricate, the small physical size of pulled disk-type electrodes makes them suitable for experiments in small spaces and as SECM tips.

In most published studies, a Sutter P-2000 laser pipette puller was used for fabricating thin-glass nanoelectrodes, and five pulling parameters in the program—heat, filament, velocity, delay, and pull—were adjusted to obtain the desired a and r_g . While general requirements for successful pulling (i.e., the use of annealed wire, thorough cleaning of the capillary and microwire, and good vacuum) are straightforward, the parameter values may not be the same for different P-2000 pullers, and even for the same instrument, they have to be adjusted occasionally to produce electrodes with the desired size and shape. The procedures were developed for fabricating different metal nanoelectrodes (Pt,²⁰ Au,^{21a} and Ag^{21b}). Producing high-quality gold and silver electrodes was found to be harder, especially for Ag, whose low melting point necessitated the use of the pulling sequence consisting of three different programs. A modified pulling procedure was also developed to produce thick-glass nanoelectrodes.²²

The next step is to expose the conductive surface to solution; in most cases, this was done by mechanical polishing. Thick-glass electrodes were polished manually on the felt polishing cloth, which was wetted with a KCl solution containing 50 nm alumina particles and connected to the external circuit with a metal clip. The effective radius of the exposed metal surface was monitored using a high-input impedance field effect transistor (MOSFET)-based circuit.¹⁹ This protocol yielded electrodes with a very small effective radius of ~ 10 nm¹⁹ and even smaller.²²

Polishing sharp, pulled nanoelectrodes is not straightforward because of the tip fragility. The original procedures based on glass etching and micropolishing were only partially successful.¹⁸ Flat disk-type Pt nanoelectrodes suitable for kinetic measurements and quantitative SECM experiments were prepared by polishing on a 50 nm lapping tape under video microscopic control.²⁰ A micromanipulator was used to move the pipette vertically toward the slowly rotating disk of the micropipette beveler. The choice of the correct separation distance such that the nanoelectrode gets polished without being broken is the most challenging part of this procedure. To prepare a nanoelectrode that can be used as an SECM tip, one has to ensure that its axis is strictly perpendicular to the polishing surface. Several modifications of the aforementioned pulling/polishing procedures have been reported. For instance, a quickly rotating quartz-sealed, pulled nanoelectrode was slowly lowered toward the surface of a fixed polishing plate.²³

An interesting alternative to mechanical polishing of sharp nanoelectrodes is the use of the focused ion beam (FIB).²⁴ In Ref. [24a], a pulled capillary containing a glass-sealed Pt wire was heat annealed by using a microforge and then milled by the FIB, producing a well-shaped, smooth disk-type nanoelectrode with a thin-glass sheath. Although, this procedure has only been reported for relatively large ($a \geq 100$ nm) nanoelectrodes, the fabrication of smaller electrodes may also be feasible.

A wider class of disk-type nanoprobe can be prepared by electrodeposition, including metals and other materials not suitable for pulling/polishing. To produce an essentially flat (rather than hemispherical) electrode, one can etch a disk-type Pt nanoelectrode and fill the resulting cavity with a metal of choice. Both sharp^{17b} and thick-wall²⁵ nanoelectrodes have been prepared in this way. To control the size of the deposited electrode, one can either try to stop the deposition process

at the moment when the nanocavity is completely filled^{17b,26} or polish away the excess metal.²⁵ The moment when the nanocavity is filled can be detected from the current transient.²⁶ The deposition current increases slowly with time as the cavity gets filled with metal; and the current–time curve becomes much steeper when the cavity depth becomes smaller than its radius. This method, however, is not exact unless the results of the deposition process can be checked by SECM or AFM (see Sections 15.2.2 and 15.2.3). Removing the excess of deposited metal by polishing is not straightforward. Extensive polishing is likely to remove the deposited metal completely, while slight polishing may result in the electrode radius significantly larger than the original disk before etching²⁵ and apparently nonflat geometry. It is also difficult to ensure the consistency of the metal/glass seal and the absence of solution leakage. Overall, the electrodeposited probes should be more useful for experiments that do not require perfect electrode geometry (e.g., potentiometric measurements²⁷ or nanoparticle attachment²⁵).

15.2.1.5 Recessed Disk and Nanopore

The possibility of a disk-type nanoelectrode surface becoming recessed into the insulator was first deduced²⁸ from the analysis of extremely fast electron-transfer (ET) rates measured in early voltammetric experiments at nanoelectrodes.^{10b} A nanoelectrode can also become recessed in the process of polishing.²⁹

In several publications, different kinds of recessed electrodes were prepared purposefully. For instance, a nanocavity formed within insulating wax was used to trap and detect single molecules.³⁰ Two extreme examples of recessed nanodisks are *slightly recessed* nanoelectrodes with the recess depth less than or comparable to the disk radius³¹ and nanopore electrodes whose recess depth is much larger than the radius.³² The former were prepared by controlled etching of nanometer-sized, flat Pt electrodes. By using high-frequency (e.g., 2–20 MHz) ac voltage, the layer of Pt as thin as ≥ 3 nm was removed to produce a cylindrical cavity inside the insulating glass sheath. The recess depth was evaluated from steady-state voltammetry and SECM approach curves,³¹ and the possibility of using AFM to measure it more accurately was shown later.²⁶ Slightly recessed electrodes were used for electrodeposition (see above) and to form ultrathin layer electrochemical cells.³³ Glass nanopore electrodes were created by first fabricating a Pt nanodisk electrode and then etching it with a low-frequency ac current to obtain a Pt disk embedded at the bottom of a conical^{32a,b} or cylindrical^{32c} pore.

15.2.2 CHARACTERIZATION OF NANO-ELECTRODES: VOLTAMMETRY AND SECM

The characterization of a nanoelectrode includes the evaluation of its effective radius, true surface area exposed to solution, and the thickness of the insulating sheath, as well as the determination of the electrode geometry. In many published studies, the electrode radius was evaluated from the steady-state diffusion limiting current assuming either hemispherical, or conical, or planar disk geometry. For a nonflat electrode, this assumption is often problematic because of essentially unavoidable imperfections of its geometry.

Steady-state voltammetry is the simplest and most popular technique employed for characterizing nanoelectrodes. The goals here are to check that the electrode response follows the basic electrochemical theory and to determine the effective radius value. Assuming that a nanoelectrode is sufficiently large to avoid deviations from conventional laws of diffusion (see Chapter 2), one can analyze the shape of steady-state voltammograms using the theory developed for micrometer-sized electrodes.³⁴ The shape of the reversible steady-state voltammogram is independent of the electrode geometry and determined by the Nernst equation.^{34a} In earlier publications, the effective radius of a nanoelectrode was typically evaluated from the diffusion limiting steady-state current assuming that it is shaped either as a hemisphere (Equation 15.1) or a disk (Equation 15.2):

$$i_{\text{hs}} = 2\pi nFDac^* \quad (15.1)$$

$$i_{\text{disk}} = 4nFDac^* \quad (15.2)$$

where

n is the number of transferred electrons

F is the Faraday constant

a is the electrode radius

D and c^* are the diffusion coefficient and bulk concentration of the reactant, respectively

Nearly perfect steady-state voltammograms of a well-behaved redox mediator (e.g., ferrocene in acetonitrile or ferrocenemethanol in aqueous solutions) at nanometer-sized electrodes have been reported by a number of research groups. A sigmoidal, retraceable curve with an essentially flat diffusion plateau and very low charging current (at potential scan rates up a few hundred millivolts per seconds; Figure 15.2a, red curve) is a good starting point in the nanoelectrode characterization; however, it does not provide any information about electrode geometry or potential problems, such as solution leakage or surface recess.

One approach to leakage detection is based on the comparison of fast-scan (e.g., ≥ 10 V/s) and slow-scan (e.g., ≤ 200 mV/s) voltammograms of the dissolved species. In the case of significant leakage, the presence of a thin layer of solution containing electroactive species inside the insulating sheath should result in peak-like features in fast-scan voltammograms, with a peak height proportional to the scan rate. By contrast, sigmoidal fast-scan voltammograms similar to the slow-scan, steady-state voltammograms—except for a moderate charging current contribution—point to the consistent seal and no solution leakage (cf. blue and red curves in Figure 15.2a). However, the apparent capacitance of a nanoelectrode is much larger than the capacitance of the metal/solution nanointerface due to *stray capacitance* of its insulated portion and wiring. Thus, detecting the leakage from capacitive current is not straightforward.

Another approach to detecting the leakage is to use fast-scan voltammetry of adsorbed species to evaluate the effective surface area of the electrode.¹⁵ In principle, one can eliminate the leakage possibility by showing the agreement between the area value and the effective radius obtained from steady-state voltammetry of dissolved redox species. However, it was difficult to use the same electrode for area measurements and kinetic experiments and to accurately measure the amount of adsorbed species for electrodes smaller than ~ 60 nm radius.¹⁵

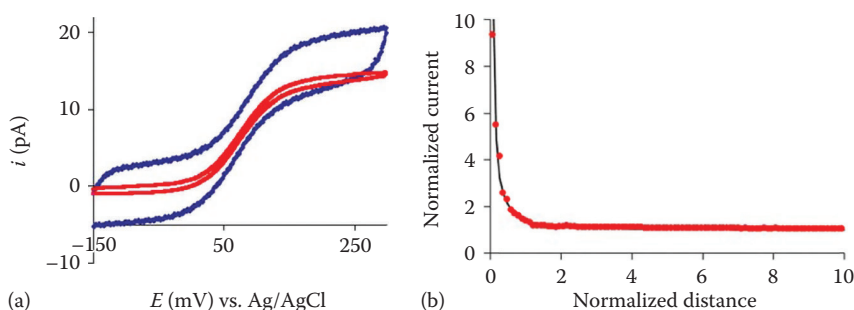


FIGURE 15.2 Characterization of a nanoelectrode by voltammetry and SECM. (a) Slow (red curve) and fast (blue curve) scan voltammograms of 1 mM FcCH_2OH at the 52 nm polished Pt electrode. $\nu = 50$ mV/s (red) and 50 V/s (blue). (b) Experimental (symbols) and theoretical (solid line) current–distance curves obtained with the same electrode as in (a) approaching an evaporated Au substrate.

More reliable characterization can be achieved by combining voltammetry with SECM, where the nanoelectrode serves as a tip (see Chapter 18 for discussion). The SECM is most useful for characterizing planar electrodes because high positive (or negative) feedback can only be obtained with a flat, well-polished tip whose entire surface can be brought close to the flat substrate. No other electrode geometry discussed earlier (i.e., conical, spherical-cap, cylindrical, or recessed disk) can yield either high positive (e.g., $I = i_T/i_{T,\infty} > 7$, where i_T is the tip current in a close proximity of the substrate surface and $i_{T,\infty}$ is its value far away from the substrate) or negative (e.g., $I \leq 0.1$) feedback. In Figure 15.2b, an SECM approach curve is fitted to the theory with $a = 52$ nm. The same a value was obtained independently from the diffusion limiting current at the same Pt electrode (Figure 15.2a). The radius value is reliable because of the high positive feedback current (up to a normalized current of ~ 9.5 , which corresponds to distance of the closest approach, $d < 5$ nm). While well-shaped SECM approach curves showing high positive (and negative) feedback in good agreement with the theory can provide strong evidence that a nanoelectrode is essentially flat, well polished, and not leaky, lower feedback often observed in current–distance curves is hard to interpret. Possible origins of such a response include either recessed or protruding tip geometry, surface contamination, or poor tip/substrate alignment. The ambiguity in interpretation of low-feedback approach curves complicates the detection of the nanometer-scale damage to the electrode,^{24a} as discussed in Section 15.2.3.

Both positive and negative feedback currents depend strongly on the height of the convex tip (i.e., one shaped as a cone or a spherical cap) or the depth of the recessed tip. Thus, the effective radius and the height of a conical/spherical nanoelectrode can be determined by fitting the experimental current vs. distance curves to the theory.¹⁴ Similarly, the depth of the recess of the conductive surface into the insulator can be evaluated from the best fit of the experimental approach curve to the theory and compared to the value obtained from steady-state voltammograms.^{31,33} Negative feedback current is more sensitive to the insulator thickness, and the r_g value can be evaluated from approach curves obtained at an insulating substrate (see Section 15.3.2). An advantage of the SECM characterization is that it is based not on the appearance of a nanoelectrode but on its current response, which is much more relevant to electrochemical measurements. However, if the tip geometry is imperfect, fitting an experimental approach curve to the theory may be problematic. One should also notice that only a sharp nanoelectrode with a thin insulating sheath can be used as an SECM tip and the reliability of the electrode characterization is largely determined by the attainable distance of the closest approach.

Presently, good-quality SECM approach curves can only be obtained using nanoelectrodes with the radii ≥ 10 nm. Several recent attempts to employ extremely small ($a < 5$ nm) electrodes for kinetic experiments,²² transport,³⁵ and nucleation¹³ studies underscore the importance of developing characterization techniques for such electrodes. Small imperfections in the geometry of these electrodes may result in misleading experimental results. For instance, a 1 nm surface recess would cause the current to a 1 nm radius electrode to be only 43% of the current to the equally sized, nonrecessed disk.

15.2.3 CHARACTERIZATION OF NANO-ELECTRODES: ELECTRON MICROSCOPY AND AFM

Several authors used SEM to evaluate the size and shape of a nanoelectrode.^{12,18–20,24,36} The SEM lateral resolution is not sufficiently high to characterize electrodes smaller than ~ 50 nm radius. Moreover, even for relatively large electrodes (e.g., $a > 50$ nm), SEM micrographs provide mostly qualitative information about electrode shape that cannot be used for quantitative modeling of its response, and insufficient z-axis resolution makes it hard to distinguish between flat, recessed, and protruding nanoelectrodes. Nevertheless, SEM images can provide important information about nanoelectrode geometry and facilitate the detection of damage to its surface. Figure 15.3 shows SEM images of the same submicrometer-sized Pt disk electrode (a) before and (b) after it was damaged by an electrostatic discharge.^{24a} The Amemiya group showed that such a damage can be caused

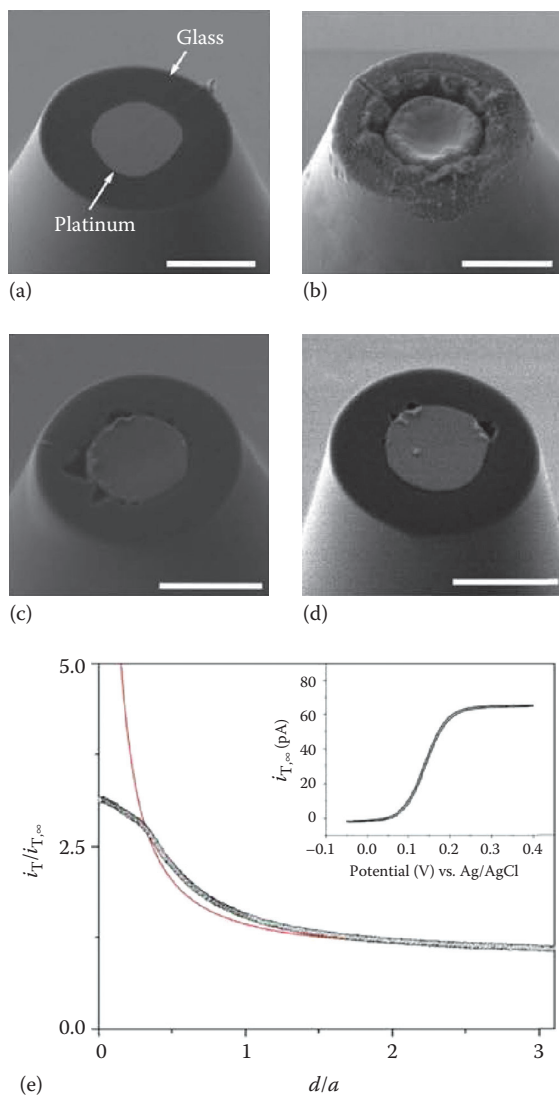


FIGURE 15.3 SEM images and electrochemical responses of a damaged glass-sealed submicrometer Pt electrode. SEM images were obtained (a) before and (b) after electrostatic discharge damage. Panels (c) and (d) show moderately and weakly damaged Pt electrodes, respectively. Scale bars, 1 μm. (e) Experimental (circles) and theoretical (solid line) SECM current–distance curves obtained with the damaged tip (panel b) approaching an unbiased Au substrate. The inset in (e) shows a steady-state voltammogram obtained at the same damaged electrode; $v = 20$ mV/s. Solution contained 0.5 mM FcMeOH in 0.1 M KCl. (Reprinted with permission from Nioradze, N., Chen, R., Kim, J., Shen, M., Santhosh, P., and Amemiya, S., Origins of nanoscale damage to glass-sealed platinum electrodes with submicrometer and nanometer size, *Anal. Chem.*, 2013, 85, 6198–6202. Copyright 2013 American Chemical Society.)

by touching an electrode or by voltage spikes produced by the potentiostat. Surprisingly, a severely damaged electrode (Figure 15.3b) yielded a nearly perfect steady-state voltammogram (inset in Figure 15.3e)—a strong indication that quantitative (especially kinetic) experiments performed at nanoelectrodes without proper characterization are likely to produce erroneous results. An attempt to detect this damage by SECM was only partially successful: the experimental approach curve in Figure 15.3e followed the conventional theory for positive feedback up to $I \approx 2.5$ and then leveled

off. Clearly, detecting less profound damage in nanoelectrodes shown in Figures 15.3c and d by SECM and voltammetry could be difficult.

TEM, which offers significantly higher resolution than SEM, is potentially useful for characterizing smaller nanoelectrodes. For instance, Li et al.²² presented TEM side views of ≤ 3 nm radius Pt wires inside the insulating sheath of their nanoelectrodes. These impressive micrographs unambiguously demonstrated that the radius of the conductive metal core is comparable to the effective value of the electrode radius obtained from the diffusion limiting current. However, to characterize the geometry of ultrasmall nanoelectrodes, one needs high-resolution images of the metal surface exposed to solution.

The possibility of AFM imaging of laser-pulled, polished nanoelectrodes was shown recently.²⁹ Although a needle-shaped electrode may not look like a suitable AFM substrate (Figure 15.4a), imaging polished Pt and Au electrodes as small as ~ 20 nm radius both in air and in liquids is

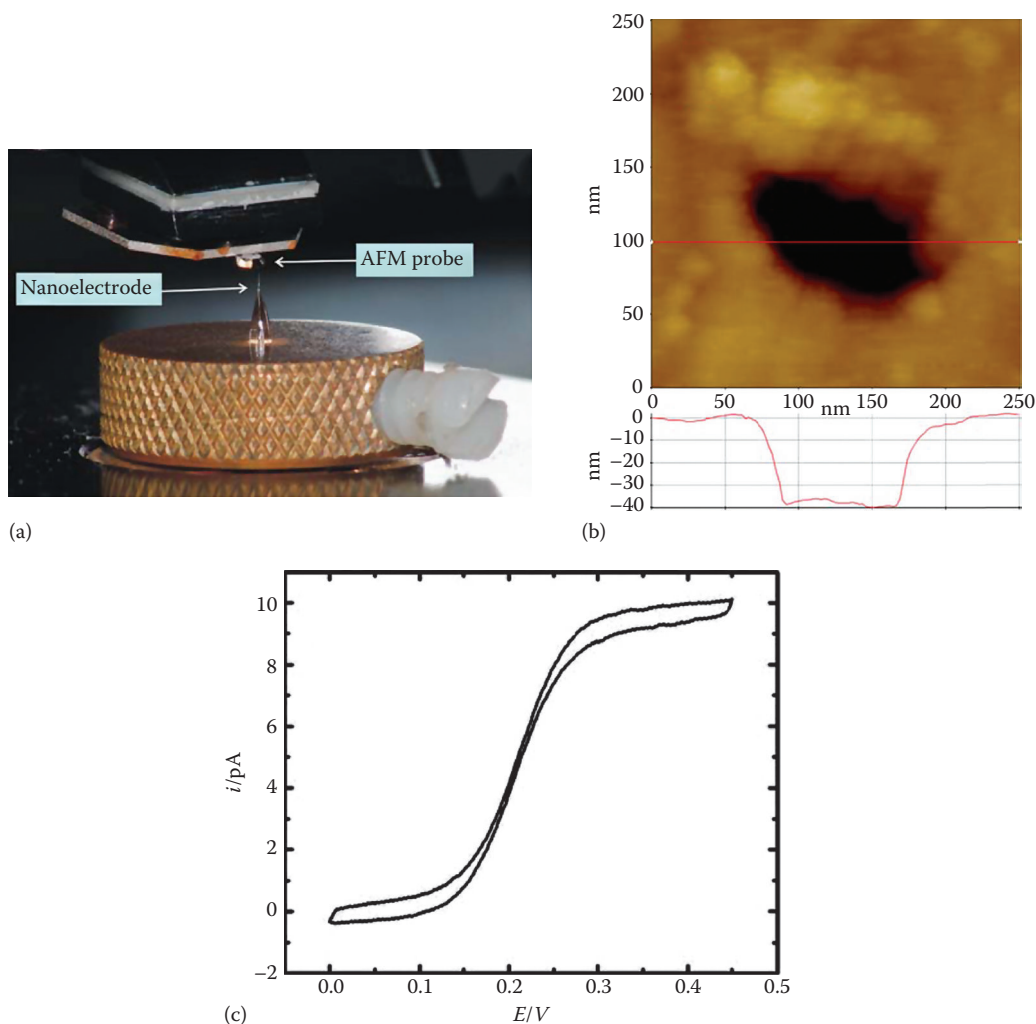


FIGURE 15.4 (a) Experimental setup used for AFM imaging of nanoelectrodes in air. A glass-sealed, polished nanoelectrode is positioned under the AFM probe. (b) Noncontact topographic image of a recessed Pt nanoelectrode in air. The scan rate was 0.5 Hz. The red line corresponds to the shown cross section. (c) Steady-state voltammogram of 1.2 mM FcCH₂OH obtained at the same electrode. $\nu = 50$ mV/s.

relatively easy. Because of its high (subnanometer) z-axis resolution and capacity for imaging in solution, AFM can provide detailed information about nanoelectrode geometry and surface reactivity that would be hard to obtain by any other technique. For example, a noncontact mode AFM image in Figure 15.4b shows a 50–55 nm radius significantly recessed electrode (~40 nm recess depth). Using the available theory (Equation 9b in Ref. [31]), one can obtain the effective value of $a = 54$ nm from the diffusion limiting current measured in 1.2 mM FcCH_2OH (Figure 15.4c) in good agreement with the radius found from Figure 15.4b. Without an AFM image, one would not be able to tell that this electrode is recessed from the voltammogram in Figure 15.4c. The effective radius calculated from this voltammogram without taking into account the recessed geometry would have been as small as 20 nm. Kinetic experiments (and other geometry-sensitive experiments) at such an electrode could yield highly inaccurate results. The cracks in the insulating sheath, which may result in solution leakage, can also be detected in noncontact AFM images.²⁹

Electrodes characterized by AFM (especially by noncontact mode imaging) are not damaged and can be employed in electrochemical experiments. The capacity of the AFM for in situ monitoring of surface reactions at nanoelectrodes was used to study nucleation/growth of Ag nanoclusters⁷ and dissolution of Pt nanoelectrodes during oxygen reduction³⁷ and to fabricate nanosensors for reactive oxygen and nitrogen species with well-defined geometry.²⁶ The main point was to visualize the changes resulting from the deposition process and compare them to the corresponding electrochemical data. The electrodeposition of Pt black under the AFM control is illustrated in Figure 15.5. A noncontact topographic image of an etched Pt electrode (Figure 15.5a) in solution before the platinization shows the effective radius, $a \approx 70$ nm, and the etched cavity depth of ≥ 16 nm. The deposition of Pt black was done by stepping the electrode potential to -100 mV vs. Ag/AgCl , while the AFM tip, immersed in the platinization solution, was scanned in x-direction above the electrode surface. Figure 15.5b shows a stack of 60 consecutive topographic 1D scans obtained over a 60 s period. The deposition was stopped by stepping the electrode potential to 0 mV after Pt black

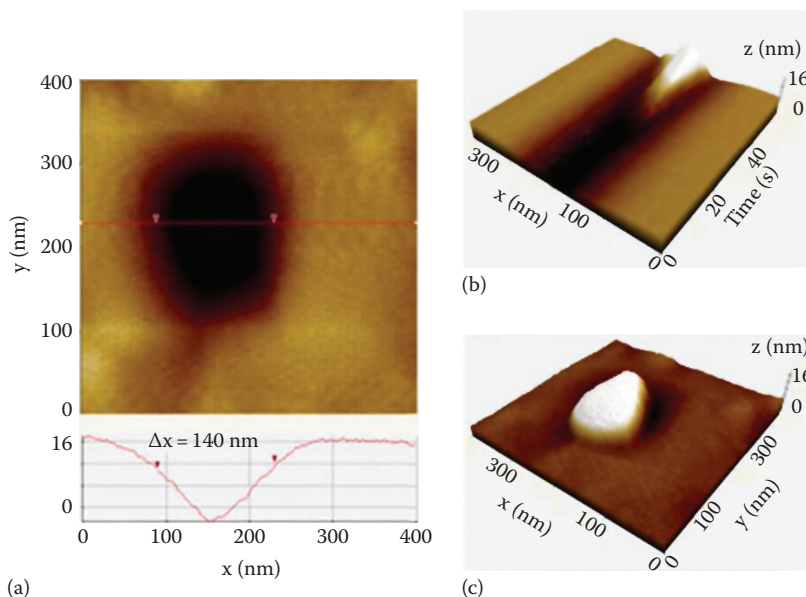


FIGURE 15.5 AFM topographic images of an etched Pt nanoelectrode in solution (a) before and (c) after the deposition of Pt black and a time evolution of a line scan (b) during the electrodeposition process. The red line in (a) corresponds to the shown cross section. (b) The tip was scanned along the x-axis with the scan rate of 1 Hz. The position of the line scan approximately corresponded to the red line in (a).

completely filled the cavity and slightly protruded (by ~15 nm) from the glass sheath, as can be seen from the image of the same electrode obtained after the platinization (Figure 15.5c). In another deposition experiment, the initial depth of the nanocavity was only ~2 nm, and the protrusion height after the deposition of Pt black was ~3 nm.²⁶

15.3 NANOPIPETTE-SUPPORTED ITIES

15.3.1 ELECTROCHEMISTRY AT NANO-ITIES

Similar to solid/liquid electrochemistry, important advantages can be obtained by replacing a macroscopic interface between two immiscible electrolyte solutions (ITIES) with a liquid/liquid nanointerface. In 1986, Taylor and Girault introduced micrometer-sized liquid/liquid interface supported at the tip of a pulled glass pipette.³⁸ Nanoscale ITIES and their arrays have later been formed by using nanopipettes, nanopores, and porous membranes.³⁹ Electrochemistry of nanopores and porous membranes is surveyed in Chapter 11; our focus here is on the ITIES supported at the tip of a nanometer-sized pipette.

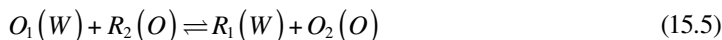
In addition to ET reactions occurring also at the metal/solution interfaces, CT reactions at the ITIES include simple and facilitated ion-transfer (IT) processes. All CT processes occurring at macroscopic ITIES can also be observed at a nanopipette-supported ITIES, including simple IT,^{40–44} facilitated IT,^{3,42,45} and ET reactions.⁴⁶ A simple IT process is a one-step reaction in which a cation I^{n+} (or an anion) is transferred directly from one phase (e.g., water) to the second phase (e.g., organic):



Facilitated IT reactions require a ligand (L^{m-}) in the organic phase (e.g., 1,2-dichloroethane, DCE), which can react with I^{n+} to form a complex, resulting in the transfer of I^{n+} :



The ET reaction between redox molecules confined to two immiscible liquid phases can be described as



Because of the negligibly small ohmic potential drop (typically, <1 mV) and low double-layer charging current, a nanopipette is an excellent tool for studying CT processes at the ITIES and nanoscale electrochemical imaging.³⁹ At first glance, it appears to be an extremely simple device; however, quantitative nanopipette voltammetry is not straightforward. It requires a well-defined nanoscopic ITIES formed at the pipette tip and thorough characterization of its geometry.

15.3.2 FABRICATION AND CHARACTERIZATION OF NANOPIPETTES

15.3.2.1 Pulling a Nanopipette

By pulling borosilicate glass or quartz capillaries with a laser pipette puller (e.g., P-2000, Sutter Instrument Co.), a pair of nanopipettes with the same orifice radius can be obtained. When choosing capillaries, one needs to consider several factors, including the material (quartz or glass) and properties of a specific capillary (e.g., the wall thickness or the presence of a filament).⁴⁷ Borosilicate glass has a relatively low melting point and requires heat (one of the P-2000 parameters) between 300 and 400, while a significantly higher heat value—between 550 and 900—is

used to pull quartz capillaries. Borosilicate glass is much less expensive than quartz and easier to use for pulling relatively large (micrometer- or submicrometer-sized) pipettes. However, ultrasmall nanopipettes with a relatively short taper, which is essential for minimizing the solution resistance, have to be fabricated from quartz. Quartz is very sensitive to uneven heating, which may result in asymmetrical pipettes. In this case, using quartz capillaries with a thicker wall (≥ 0.5 mm) can help. The ratio of the outer and inner diameters of the capillary largely determines the RG of pulled nanopipettes ($RG = r_g/a$, where r_g is the glass radius at the tip and a is the radius of the orifice).

To support an ITIES, a nanopipette has to be filled with solution. Using capillaries with filaments makes it easier to bring aqueous solution to the end of the pipette tip; otherwise, it is difficult to remove the air and to fill the nanopipette completely. Capillaries without filaments can be used to produce pipettes that will be filled with organic solution. Organic solvents, such as DCE, are relatively easy to inject in a glass or quartz pipettes, and at the same time, the solvent evaporation is slower in the absence of a filament.

The pulling process is controlled by adjusting five parameters in the puller program, which are heat, filament, velocity, delay, and pull. To obtain smaller tips, one can increase the value of heat, velocity, or pull or decrease the value of filament or delay. To control the length of the taper while maintaining the nanometer-scale tip diameter, one can limit the value of velocity and increase pull at the same time. The roughness of the pipette tip can be reduced by polishing^{48a} or by FIB milling.^{48b} A potential problem is that the pipette orifice can be contaminated by polishing agent.

15.3.2.2 Surface Modification

When a water-filled glass or quartz pipette is immersed in organic solution, a thin aqueous film forms on its hydrophilic outer wall, making the true area of the liquid/liquid interface much larger than the geometrical area of the pipette orifice.⁴⁹ The film formation can be avoided by silanizing the outer pipette wall to render it hydrophobic while keeping the interior wall nonsilanized. In most early publications, this was done by dipping the pipette tip into silanizing agent (typically, chlorotrimethylsilane) while passing a flow of argon through the pipette. This procedure is straightforward for micrometer-sized pipettes, but not easy for nanopipettes.^{40,46} Silanization of smaller pipettes must be done cautiously to avoid the formation of a film on the inner wall, which can partially block the pipette orifice and induce solvent penetration into its narrow shaft. A recently developed protocol for silanizing pipettes in the vapor phase allows one to avoid oversilanization of relatively small (e.g., ~ 10 nm radius) pipettes⁴³; however, the possibility of silanizing even smaller (e.g., $1\text{--}5$ nm⁴²) pipettes is uncertain.

When the pipette is filled with organic solution and immersed in the aqueous phase, its inner wall needs to be silanized to avoid water penetration into the pipette. This can be done by dipping the tip into chlorotrimethylsilane for $5\text{--}7$ s.⁵⁰ In this case, both the outer and inner walls of the pipette get silanized, but unlike water, organic solution is not likely to form a layer on the outer wall even though it becomes hydrophobic.⁴⁹ A more controlled method for vapor silanization was reported recently.⁵¹ The pipettes were fixed in a minivacuum desiccator, which was first evacuated by the pump, and then the vapor of highly pure *N*-dimethyltrimethyl silylamine was delivered from the flask to the desiccator, where the pipettes were exposed to it for about 15 min.

15.3.2.3 Characterization of Nanopipettes

Checking a nanopipette with an optical microscope is useful for initial evaluation of its properties (i.e., straight or bent, not broken, order of magnitude estimate of the tip diameter). However, the tip of a nanopipette is too small to be quantitatively characterized by optical microscopy. The main parameters defining the pipette geometry are the radius, a ; the glass thickness at the tip, r_g (the related dimensionless parameter is $RG = r_g/a$); and the pipette angle, θ_p (Figure 15.6).

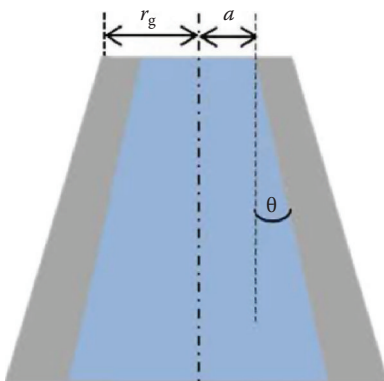


FIGURE 15.6 Schematic diagram of the nanopipette geometry.

The most commonly used methods for characterizing nanopipettes are electron microscopy (SEM and TEM) and electrochemical techniques (cyclic voltammetry and SECM). SEM is a direct way of visualizing the pipette geometry, but it is limited by the resolution of the instrument. For pipettes with diameters smaller than ~ 50 nm, it is difficult to see the orifice clearly, and a few nanometers thick conductive coating (e.g., Au or Pd) has to be applied to image the insulating nanotip without significant charging. Nevertheless, SEM can provide important information about pipette size and geometry. For instance, both a and r_g of a correctly silanized nanopipette in Figure 15.7a are very similar to those of a nonsilanized pipette (Figure 15.7b), which was pulled from the same quartz capillary; and therefore no orifice blocking occurred during silanization.

Although not as widely used as SEM, TEM can be very useful for characterizing nanopipettes. Unlike metal electrodes, the liquid–liquid interface is supposed to be featureless, and imaging it is not essential for pipette characterization. A high-resolution side view of a nanopipette can be used to evaluate its radius, R_G , and θ_p , which are ~ 55 nm, 1.4, and 6° , respectively, for the pipette imaged in Figure 15.8.

Similar to metal nanoelectrodes, the size and the geometry of a nanopipette can be examined by AFM; however, obtaining high-quality images of small and sharp pipettes with $R_G < 2$ can be difficult because of the stability issues.

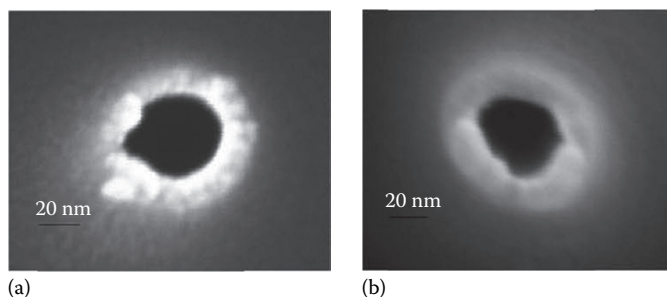


FIGURE 15.7 Top view of SEM images of (a) silanized and (b) nonsilanized nanopipettes pulled from the same quartz capillary. (Reprinted with permission from Wang, Y., Velmurugan, J., Mirkin, M.V., Rodgers, P.J., Kim, J., and Amemiya, S., Kinetic study of rapid transfer of tetraethylammonium at the 1,2-dichloroethane/water interface by nanopipette voltammetry of common ion, *Anal. Chem.*, 2010, 82, 77–83. Copyright 2010 American Chemical Society.)

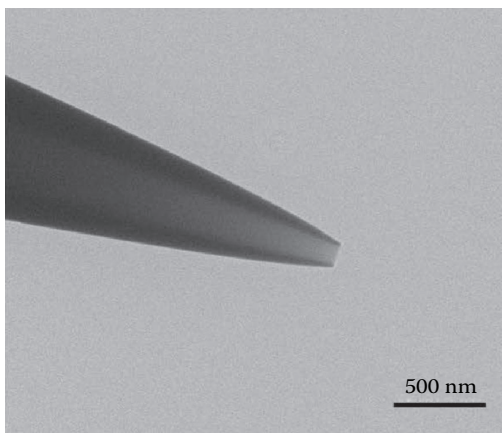


FIGURE 15.8 TEM image of a quartz nanopipette.

Steady-state voltammetry of IT from the external liquid phase to the filling solution has often been used to evaluate a from the diffusion limiting current. The radius of a nonsilanized nanopipette can be found from Equation 15.6 proposed by Beattie et al.⁵²:

$$i_2 = 3.35\pi zFD_2c_2^*a \quad (15.6)$$

where z , D_2 , and c_2^* are the charge of the transferred ion, its diffusion coefficient, and bulk concentration in the external solution (phase 2). Sometimes, the background subtraction is necessary to obtain accurate results. One should also keep in mind that Equation 15.6 is an approximate equation obtained empirically for micrometer-sized pipettes. Verifying its accuracy for nanopipettes is difficult.

The equation for the diffusion limiting steady-state current to the orifice of a silanized pipette is more exact:

$$i_2 = 4xzFD_2c_2^*a \quad (15.7)$$

where x is a function of the dimensionless glass radius, RG, which was tabulated^{53a} and expressed by an analytical approximation for disk-shaped interfaces.^{53b} Either a or RG can be found from Equation 15.7 if the second parameter is known. The RG value can be found independently from an SECM approach curve by using the nanopipette as a tip^{40,48a} (for discussion, see Chapter 18). A good fit of SECM negative feedback approach curve to the theory can also confirm that the ITIES is essentially flat and not recessed. Pipettes as small as ~8 nm radius with RG = 1.6 have been characterized in this way.^{48a}

If a transferable ion is initially present in the filling solution, the IT current is determined by diffusion inside the pipette. The geometry of the pipette inside can be approximately described by two parameters, a and θ_p (Figure 15.6), which can be evaluated from the steady-state limiting current of the ion egress⁴³:

$$i_1 = 4f(\theta_p)zFD_1c_1^*a \quad (15.8)$$

where D_1 and c_1^* are the diffusion coefficient and bulk concentration of the transferable ion in the filling solution (phase 1) and $f(\theta_p)$ is a function of the tip inner angle, θ_p , as given by^{43,54}

$$f(\theta_p) = 0.0023113912 + 0.013191803\theta_p + 0.00031738596\theta_p^{1.5} - 5.8554625 \times 10^{-5}\theta_p^2 \quad (15.9)$$

The pipette resistance is another important parameter to be measured if the pipette is to be used in kinetic experiments (and also for resistive-pulse sensing or scanning ion conductance microscopy, SICM).⁵⁵ The total pipette resistance ($R_T = R_{\text{int}} + R_{\text{ext}}$) comprises of two components, that is, the resistances of the inner and outer solutions. It can be obtained from the slope of a current vs. voltage curve recorded with the same solution inside and outside the pipette.^{55a} Such curves are normally linear for larger (e.g., $a \geq 100$ nm; the exact limit depends on the ionic strength of solution) pipettes, but nonlinear for smaller pipettes. In the latter case, the slope can be determined from the essentially linear low-voltage portion of the curve (e.g., ± 20 mV^{56b}). Assuming that the pipette orifice is disk shaped, $R_{\text{ext}} = 1/(4\kappa a)$ is entirely determined by its radius and solution conductivity (κ). The internal pipette resistance ($R_{\text{int}} = R_T - R_{\text{ext}}$) can be related to θ_p by a simple analytical approximation^{56a}

$$R_{\text{int}} = \frac{1}{\kappa \pi a \tan \theta} \quad (15.10)$$

which can be used to evaluate the pipette angle.^{56b}

15.3.3 ELECTROCHEMICAL MEASUREMENTS AT NANOPIPETTES

Unlike macroscopic ITIES, in nanopipette voltammetry, the interfacial ET or IT current is very small (pA range). Therefore, potentiostatic experiments at the nano-ITIES are performed by applying voltage between two reference electrodes, and a four-electrode potentiostat is not required. Typically, the potential gradient and the ohmic potential drop inside a pipette are too small for significant electromigration or electro-osmotic flow along its charged inner wall.^{3,43,54} The electrostatic and double-layer effects can be more significant for smaller nanopipettes, for example, $a \leq 5$ nm.⁴²

Choosing a proper potential sweep rate (ν) in pipette voltammetry is essential for attaining a steady-state and sufficiently low charging current. Computer simulations and experiments showed that ion diffusion on either side of the nano-ITIES reaches a steady state during a potential cycle at a moderate ν .^{43,54,57} The related dimensionless parameter $\sigma = (a^2/4D_2)(z_i F \nu / RT)$ compares a to the diffusion distance in the external solution, $\sqrt{D_2 RT / z_i F \nu}$. It was suggested that the IT process attains a steady state if $\sigma \ll \sim 10^{-4}$.⁵⁴ In a typical voltammetric experiment at a nanopipette, $\nu = 10$ mV/s, $a = 50$ nm, and $D_2 = 10^{-5}$ cm²/s correspond to a very small σ value of 2.4×10^{-7} , and steady state is readily attained in both liquid phases.

One should notice, however, that the σ value reflects the diffusion only in the external solution. The radial diffusion of ions from the external solution to the tip is much less hindered by the glass wall than the diffusion inside a tapered pipette. The time required to attain a steady state is typically determined by the mass-transfer rate inside the pipette and the geometry of the pipette inside. Thus, besides the tip inner radius (which is included in the dimensionless parameter σ), θ_p can also influence the attainment of a steady state. In practice, the variations in θ for quartz nanopipettes are relatively small, that is, from $\sim 4^\circ$ to $\sim 20^\circ$, and sigmoidal forward and reverse waves that completely retrace each other can be obtained at moderate scan rates (e.g., $\nu \leq 1$ V/s for $D \approx 10^{-5}$ cm²/s), thereby confirming the apparent steady state on both sides of the nanopipette tip.

It was noted^{43a} that transient cyclic voltammetry is not practical with nanopipettes. A σ value of $>10^{-4}$ is required for obtaining a transient cyclic voltammogram (CV) of simple IT even at a narrow pipette with the taper angle of $\sim 6^\circ$. This corresponds to $\nu > 4$ V/s, assuming $z = 1$, $a = 50$ nm, and $D_2 = 10^{-5}$ cm²/s. At such a fast potential sweep, a large capacitive current (mostly due to stray capacitance of a nanopipette) would severely distort a voltammogram (Figure 15.9b). Transient CVs can be obtained at larger (micrometer-sized) pipettes.

The preceding discussion assumes that the diffusion coefficients of the transferred ion are similar inside the pipette and in the outer solution. However, a very slow diffusivity (e.g., in ionic liquid [IL]⁴⁴) can result in a significantly longer time required for the IT to reach a steady state in the external solution. Figure 15.9a shows two CVs obtained at a 500 nm pipette. At $\nu = 1$ mV/s, both egress

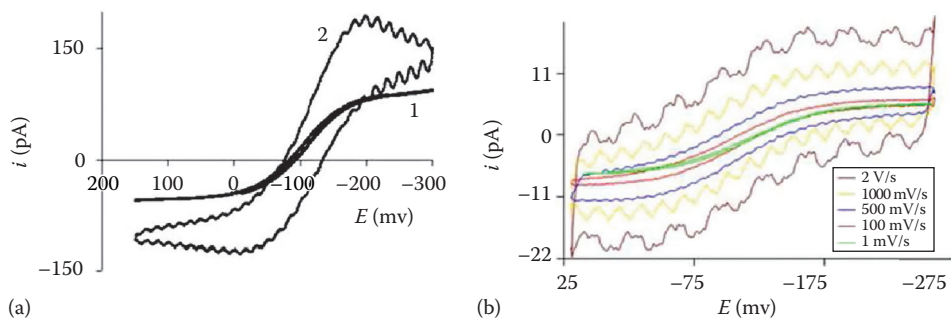


FIGURE 15.9 Effect of the potential sweep rate on CVs of TBA⁺ transfer at the nanopipette-supported water/IL interface. (a) $a = 500$ nm. ν , mV/s = 1 (1) and 1000 (2). (b) $a = 60$ nm. ν was varied between 1 mV/s and 2 V/s, as shown in the color legend. (Reprinted with permission from Wang, Y., Kakiuchi, T., Yasui, Y., and Mirkin, M.V., Kinetics of ion transfer at the ionic liquid/water nanointerface, *J. Am. Chem. Soc.*, 2010, 132, 16945–16952. Copyright 2010 American Chemical Society.)

and ingress currents in curve 1 attain a steady state; however, at $\nu = 1$ V/s (curve 2), the egress wave remains essentially sigmoidal, while the ingress wave is peak shaped. At higher ν , the charging current becomes significant (Figure 15.9b).

15.4 KINETICS OF CHARGE-TRANSFER REACTIONS AT THE NANOINTERFACES

Steady-state voltammetry at nanometer-sized interfaces is one of the best techniques for studying fast electrochemical kinetics. Its advantages over the transient methods include the absence of limitations caused by the charging current and ohmic potential drop, relative insensitivity to low levels of reactant adsorption, and relative simplicity of data acquisition and analysis. The size of a nanointerface is the origin of these advantages and also of numerous technical difficulties, some of which are considered as follows.

15.4.1 MASS-TRANSFER AND KINETIC MEASUREMENTS AT NANOINTERFACES

The CT rate constant can be measured only if it is smaller than or comparable to the mass-transfer coefficient, m . For uniformly accessible solid/liquid or liquid/liquid interfaces, the mass-transfer coefficient can be defined as⁵⁸

$$m = \frac{i_d}{(nFAc^*)} \quad (15.11)$$

where

i_d is the characteristic mass-transfer current for a specific electrochemical method, for example, diffusion limiting current in steady-state voltammetry

A is the interfacial area

c^* is the bulk concentration of the reactant

For a disk-type interface (as well as ones shaped as a cone, a ring, or a spherical cap) under steady-state conditions, $m \sim D/a$. Thus, an important feature of nanoelectrodes (and nanopipette-supported liquid interfaces) is a very high steady-state mass-transfer rate. For example, with $D = 10^{-5}$ cm²/s, $a = 10$ nm corresponds to $m = 10$ cm/s. This gives the upper limit for the determinable rate constant of ~ 50 cm/s.

Assuming Butler–Volmer kinetics, Equation 15.12 describes the shape of a steady-state voltammogram produced by CT at any uniformly accessible electrochemical interface (i.e., when the surface concentrations and diffusion fluxes of electroactive species are uniform over the entire interfacial area)⁵⁸:

$$\frac{i}{i_d} = \frac{1}{\theta + 1/\kappa} \quad (15.12)$$

This equation is applicable to ET at the metal/solution interface and to IT at the nano-ITIES if the diffusion inside the pipette shaft does not have to be taken into account. In the former case, $\theta = 1 + \exp[nF(E - E^0)/RT]m_O/m_R$ and $\kappa = k^0 \exp[-\alpha nF(E - E^0)/RT]/m_O$ for the reduction reaction, where m_O and m_R represent mass-transfer coefficients of oxidized and reduced species, respectively, E is the electrode potential, and E^0 is the formal potential of the redox couple and k^0 and α are the standard rate constant and the transfer coefficient, respectively. For IT from the external organic solution (phase 2) to the aqueous solution (phase 1), $\theta = 1 + \exp[(\Delta_o^w \varphi - \Delta_o^w \varphi^0)zF/RT]D_2/D_1$ and $\kappa = k^0 \exp[-\alpha(\Delta_o^w \varphi - \Delta_o^w \varphi^0)zF/RT]/m_2$, where $\Delta_o^w \varphi$ and $\Delta_o^w \varphi^0$ are the Galvani potential difference across the ITIES and its standard value for the given IT, respectively, and m_2 is the mass-transfer coefficient in the outer solution. Conceptually similar equations were derived for a nonuniformly accessible disk-shaped interface⁵⁹ and SECM.²⁰

High mass-transfer rates under steady state can also be attained when two electrodes are separated by a nanoscale gap in either a thin-layer cell (TLC) or a SECM. In this case, the mass-transfer rate is a function of the separation distance, d , and $m \sim D/d$ if $d < a$.

In liquid/liquid electrochemistry, the rates of simple and facilitated IT and ET were determined from steady-state voltammograms obtained using nanopipettes filled with an aqueous solution (the resistance of an organic-filled pipette is usually too high to attain the ohmic potential drop of <1 mV required for reliable kinetic measurements³). In early experiments, the ion of interest was initially present only in one phase (either aqueous or organic), and its transfer across the ITIES produced sigmoidal voltammograms, which were used to extract kinetic parameters. In the case of a facilitated IT Equation 15.4, an excess amount of the transferable ion was added to the pipette to deplete a ligand in the external solution. The essentially spherical diffusion of a ligand species to the pipette orifice resulted in the true steady-state voltammogram. The kinetic parameters were extracted either by fitting the entire voltammogram to Equation 15.12 (or to the corresponding equation for quasi-reversible steady-state voltammogram at a disk-shaped interface⁵⁹) or by using the three-point method based on the determination of the half-wave potential, $E_{1/2}$, and two quartile potentials, $E_{1/4}$ and $E_{3/4}$.⁶⁰ The same approaches were used for the analysis of steady-state voltammograms of ET obtained at the nano-ITIES.

The asymmetry of the diffusion field at a pipette-based ITIES is important for studies of simple IT processes (Equation 15.3). With a small taper angle, the diffusion inside the narrow shaft is almost linear in contrast to the spherical diffusion of ions to the pipette orifice in the outer solution, which makes the mass transport more complicated.^{41,54,57} Depending on experimental conditions, simple IT at a nanopipette may yield either a sigmoidal and retraceable steady-state voltammetric curve or an asymmetrical, transient voltammogram.^{40–42} The latter consists of an apparently steady-state, sigmoidal wave corresponding to ingress of an ion into the pipette and a time-dependent, peak-shaped wave produced by egress of the same ion to the external solution.⁶¹

In earlier studies, sigmoidal waves of simple IT were treated using simple steady-state theory (e.g., Equation 15.12) and assuming that their shape is independent of geometry of the pipette inside. More recent simulations and experiments^{54,57} showed that this simplification is not realistic, and the reversible half-wave potential of simple IT from the external solution to the pipette under steady state depends on pipette angle, θ_p . It was suggested that kinetic and thermodynamic parameters of simple ITs determined without taking into account the effects of ion diffusion in the inner shaft of a nanopipette may not be accurate.

Another issue complicating kinetic analysis of rapid CT reactions is a weak dependence of the shape of an almost reversible steady-state voltammogram on kinetic parameters and, consequently, the lack of the unique fit between the theoretical and experimental curves. This problem was addressed by using common ion voltammetry⁴³ (see Section 15.4.4).

15.4.2 KINETICS OF ELECTRON-TRANSFER REACTIONS AT THE NANO-ELECTRODES

ET kinetics at nanometer-sized electrodes have been measured either by steady-state voltammetry or by using a nanoelectrode as an SECM tip; the latter approach is discussed in Chapter 18. Voltammetric kinetic experiments have been carried at polished, flat electrodes as well as at nonpolishable conical or spherical-type tips.^{15,22,62} Polished electrodes with a $RG \leq 10$ have been employed as SECM tips for feedback mode kinetic experiments.^{20,21a}

Watkins et al.¹⁵ measured the kinetics of ferrocenylmethyltrimethylammonium (TMAFc^+) oxidation at 19 quasi-hemispherical Pt electrodes with the effective radius varied between 2 and 150 nm. This work shows how hard it is to make kinetic measurements at nonflat nanoelectrodes. Despite major efforts made to characterize the electrode size and shape (see Section 15.2.2) and a large number of analyzed voltammograms, a significant uncertainty in the determined rate constant ($k^0 = 4.8 \pm 3$ cm/s) was apparently due to imperfect electrode geometry. No strong correlation was found between the electrode size and the measured kinetic parameters even for the radii as small as $a \leq 10$ nm, for which such correlation can be expected from existing theory⁶³ (see Chapter 2 for discussion). Another important lesson to be learned from Ref. [15] is that an individual kinetic experiment at a nanometer-sized electrode may not be reliable. To ensure that the results are meaningful, one has to treat a number of CVs obtained for a wide range of experimental conditions.

Similar quasi-hemispherical Pt electrodes were used to study kinetics of IrCl_6^{3-} oxidation in 0.5 M KCl.⁶² The electrode radii in this case were somewhat larger (48–654 nm), which may be the reason for much smaller uncertainties in the measured kinetic parameters ($k^0 = 2.9 \pm 0.2$; $\alpha = 0.50 \pm 0.01$). The authors have stressed significant deviations of the nanoelectrode responses from the classical theory observed in the absence of the supporting electrolyte and additional complications caused by ion pairing. However, no effect of the electrode size on the measured ET rate with excess KCl was reported, and the k^0 values measured at nanoelectrodes were similar to those obtained at larger electrodes in Ref. [62] and in the literature. One should also notice that the oxidation of IrCl_6^{3-} occurs at potentials sufficiently positive for formation of Pt oxide, which could have affected the ET rate.

Another kinetic study³⁶ employed nonflat Pt–Ir electrodes with the effective radii ranging from extremely small (e.g., 1.1 nm) to relatively large (e.g., 150 nm). The k^0 values were determined for $\text{FcTMA}^{2+}/\text{FcTMA}^+$ (1.1–11.9 cm/s) and $\text{Fe}(\text{CN})_6^{3-}/\text{Fe}(\text{CN})_6^{4-}$ (0.12–17.3 cm/s) redox couples. Unlike other published results, the measured rate constants for both ET reactions increased markedly (i.e., by about one and two orders of magnitude, for $\text{FcTMA}^{2+}/$ and $\text{Fe}(\text{CN})_6^{3-}/$, respectively) with decreasing a value. Moreover, the k^0 values obtained for the former reaction at larger nanoelectrodes were several times lower than those measured in Ref. [15] for the same reaction and for oxidation of either aqueous ferrocenemethanol (FcMeOH)^{20,21a} or ferrocenedimethanol ($\text{Fc}(\text{MeOH})_2$) in KCl.^{64a} In addition to uncertainties in electrode geometry, these results may have been affected by unusual approach to data analysis. The voltammograms were obtained in solution containing both oxidized and reduced forms of redox species, and only a small portion of each curve, corresponding to low (≤ 5 mV) overpotentials, was analyzed. The diffuse double-layer effects were assumed to be negligible at low overpotentials. The validity of this assumption is not obvious because the equilibrium potential is not necessarily close to the potential of zero charge. Moreover, the developed approach did not allow the authors to evaluate α and to check whether experimental curves were in agreement with the voltammetric theory.

No strong correlation between the electrode radius and kinetic parameters was found with glass-sealed, polished, thick-glass nanoelectrodes.²² The average rate constant values determined for the oxidations of Fc in acetonitrile (3.4–13.4 cm/s), FcMeOH in aqueous 0.1 M NaCl (0.5–18.8 cm/s),

and IrCl_6^{3-} in 0.2 M KCl (0.5–13 cm/s) were close to those found by other groups. However, the variation in k^0 was significant—more than an order of magnitude for the oxidation of FcMeOH—and the determined α values (0.72–0.85) were much higher than $\alpha=0.5$ expected from classical ET theory and also higher than the experimental values reported by others.

In addition to characterizing the electrode geometry (Section 15.2.2), using the SECM, one can further increase the mass-transfer rate by bringing a nanoelectrode tip very close to the surface of the conductive substrate. In this way, the kinetic parameters were determined for several rapid ET reactions—the oxidation of FcMeOH in 0.2 M NaCl ($k^0=6.8\pm0.7$ cm/s; $\alpha=0.42\pm0.03$), the reduction of 7,7,8,8-tetracyanoquinodimethane (TCNQ; $k^0=1.1\pm0.04$ cm/s; $\alpha=0.42\pm0.02$), the oxidation of ferrocene in acetonitrile ($k^0=8.4\pm0.2$ cm/s; $\alpha=0.47\pm0.02$), and the reduction of $\text{Ru}(\text{NH}_3)_6^{3+}$ in 0.5 M KCl ($k^0=17.0\pm0.9$ cm/s; $\alpha=0.45\pm0.03$) at Pt.²⁰ The kinetic parameters were found to be essentially independent of m , which was varied by two orders of magnitude by changing both a and d . In a similar manner, the kinetics of the same ET reactions (plus the oxidation of tetrathiafulvalene in DCE) were measured at Au nanoelectrodes and compared to those studied at Pt tips.^{21a} Very similar k^0 and α values were obtained with Pt and Au polished electrodes for all investigated redox species except the reduction of $\text{Ru}(\text{NH}_3)_6^{3+}$, which was found to be somewhat faster at Pt than at Au with either KCl or KF used as a supporting electrolyte; it was concluded that this reaction is not fully adiabatic.

More recently, the theory was developed^{65a} and experiments were carried out^{65b} to probe rapid ET kinetics at a macroscopic SECM substrate by quasi-steady-state voltammetry using a submicrometer-sized tip positioned at a nanometer-scale distance from the substrate surface. These results are further discussed in Chapter 18.

The nanoelectrochemical ET experiments surveyed in this section involved a number of redox couples, different supporting electrolytes, and several solvents. Surprisingly, most measured k^0 values (except for a few values obtained at poorly characterized electrodes) are within one order of magnitude range. By contrast, the homogeneous self-exchange rate constants of the same redox species cover the range of more than six orders of magnitude (e.g., from $\sim 10^3$ M/s for $\text{Ru}(\text{NH}_3)_6^{3/2+}$ to 10^9 M/s for TCNQ/TCNQ[−]). Moreover, no direct correlation between the homogeneous and heterogeneous rate constants expected from the Marcus formula was found. There are also no striking differences between the rate constants measured by different nanoelectrochemical techniques and at nanoelectrodes of different size. In general, the ET rate constants measured at nanoelectrodes are much larger than the values obtained for the same processes at macroscopic and micrometer-sized interfaces. It is not yet clear whether the observed faster rates are due to the improved capabilities for measuring fast kinetics or fundamental differences between ET processes at nanoscopic and macroscopic interfaces⁶⁶ (see Chapters 1 and 2) or experimental issues inherent in nanoelectrochemical kinetic studies.

15.4.3 KINETICS OF CHARGE-TRANSFER REACTIONS AT THE NANO-ITIES

15.4.3.1 Electron-Transfer Kinetics

ET measurements at nanopipette-supported polarizable ITIES are challenging because of interfering IT reactions and/or interfacial precipitation.³⁹ Steady-state voltammetry was used to investigate ET reactions at the polarizable ITIES formed at the tip of 50–400 nm radius pipettes.⁴⁶ Each pipette was filled with an aqueous solution containing a mixture of two forms of redox species (O_1 and R_1) and immersed in organic solution containing water-insoluble redox species (O_2). The application of a sufficiently negative potential to the internal reference electrode with respect to the external (organic) reference resulted in the electric current across the nano-ITIES due to the interfacial ET between R_1 and O_2 species. The condition $c_{R_1} \gg c_{O_2}$ was maintained in all experiments, so that the diffusion of R_1 species inside the pipette was negligible and did not control the overall current and the aqueous phase showed a metal-like behavior.⁶⁷ Steady-state

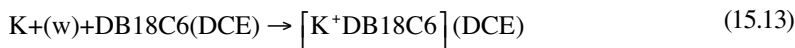
voltammograms obtained by varying the voltage applied across the ITIES were similar to those recorded at the metal/solution nanointerfaces.

By exploring a number of combinations of aqueous and organic redox couples and different supporting electrolytes, two experimental systems—the reduction of TCNQ in DCE by aqueous $\text{Ru}(\text{NH}_3)_6^{2+}$ and the ET between $\text{Fe}(\text{EDTA})^{2-}$ and TCNQ—were shown to be suitable for such studies, while all other systems failed to yield high-quality voltammograms.⁴⁶ The kinetic parameters obtained in this way for the former ET reaction ($k_{12}^0 = 2.75 \text{ M/cm/s}$ and $\alpha = 0.53$) were thought to be less reliable because of significant sensitivity of $\text{Ru}(\text{NH}_3)_6^{2+}$ species to oxygen. An extensive set of data was obtained for the TCNQ reduction by $\text{Fe}(\text{EDTA})^{2-}$.

Steady-state voltammograms obtained for this ET reaction were further improved by background subtraction and fitted to theoretical curves calculated either for a microdisk geometry or for a uniformly accessible ITIES (Equation 15.12). Kinetic parameters were obtained for different concentrations of organic and aqueous redox species and for a range of pipette radii (~50 to ~350 nm). While the determined α values were close to 0.5 and essentially independent of a and concentrations of redox species, the bimolecular standard rate constants were much larger than the values previously measured for any ET macroscopic polarized interfaces and at micrometer-sized nonpolarized ITIES. More surprisingly, the apparent k^0 increased markedly with decreasing pipette radius (i.e., from ~0.4 cm/s at $a = 300 \text{ nm}$ to ~1.8 cm/s at $a = 50 \text{ nm}$). The authors noted that this behavior is at variance with existing ET theories. They eliminated the possibilities of the recessed interface, incorrectly determined pipette radius, and other artifacts by thoroughly characterizing nanopipettes (including SECM experiments with conductive and insulating substrates; see Chapter 18). However, other factors, including the lack of the unique fit between the theoretical and experimental steady-state voltammograms and possible double-layer effects, may have affected the determined kinetic parameters. The scarcity of the available literature data precluded the comparison of the measured ET rates to those determined for the same ET reactions at larger ITIES.

15.4.3.2 Ion-Transfer Kinetics

The rates of most IT processes are too fast to be accurately measured at either macroscopic- or micrometer-sized interfaces. In contrast, the mass-transfer coefficient for a 10 nm radius pipette is $\geq 10 \text{ cm/s}$ (assuming $D = 10^{-5} \text{ cm}^2/\text{s}$), and the corresponding upper limit for the determinable heterogeneous rate constant is ~50 cm/s. The first IT kinetics studied at the nanopipette-supported ITIES was that of potassium transfer from the aqueous filling solution to DCE facilitated by dibenzo-18-crown-6 (DB18C6)³:



The mass-transfer rate was sufficiently high to measure the rate constant of potassium transfer under steady-state conditions using pipettes with $a \leq 250 \text{ nm}$. Assuming uniform accessibility of the ITIES, k^0 and α values were found by fitting the experimental data to Equation 15.12. Additionally, the kinetic parameters were evaluated by the three-point method.⁶⁰ A number of voltammograms obtained at 5–250 nm pipettes yielded $k^0 = 1.3 \pm 0.6 \text{ cm/s}$ and $\alpha = 0.4 \pm 0.1$, and no apparent correlation was found between the measured rate constant and the pipette radius. The determined k^0 was significantly higher than rate constants measured for this reaction at larger interfaces, thus providing the first evidence that the IT rates may be faster than it appeared from earlier experiments.

Yuan and Shao investigated the kinetics of several alkali metal ITs facilitated by DB18C6 at the water/DCE nanointerfaces.⁴⁵ Their measurements yielded the rate constant for potassium transfer similar to that reported in Ref. [3]. Well-shaped steady-state voltammograms were also obtained for other alkali metal cations, but the kinetic parameters determined for Li^+ , Rb^+ , and Cs^+ showed significant correlation with the pipette radius. A similar approach was used by the same group to

measure the kinetics of alkali metal transfers across the water/DCE interface facilitated with *N*-(2-tosylamino)-isopentyl-monoaza-15-crown-5.⁶⁸ The association constants were measured for alkali metal complexes in DCE, and the selectivity of this ionophore was shown to follow the sequence $\text{Na}^+ > \text{Li}^+ > \text{K}^+ > \text{Rb}^+ > \text{Cs}^+$. The standard rate constants determined from steady-state voltammograms were similar for all studied cations (~ 0.5 cm/s) and somewhat lower than those measured with DB18C6 for K^+ and Na^+ .^{3,45}

Two sources of error, which may have affected the accuracy of the results reported in Refs. [3,45], were identified in later studies. One of them is the lack of silanization of the outer pipette wall. The formation of a thin aqueous film on the hydrophilic glass surface may have resulted in the true ITIES area significantly larger than that evaluated from the diffusion limiting current (see Section 15.3.2). This should have resulted in overestimated values of the mass-transfer coefficient and standard rate constants calculated from the dimensionless parameter $\lambda = k^0/m$. Another source of error—the uncertainty in fitting experimental IT voltammograms to the theory—is discussed in Section 15.4.4.

The first attempt to measure kinetics of two rapid simple ITs at the water/DCE interface formed at the tip of a nanopipette was reported by Cai et al.⁴⁰ Employing 10–300 nm radius pipettes, $k^0 = 2.3$ cm/s was found from quasi-steady-state voltammograms of the TEA^+ transfer from DCE to the aqueous filling solution, and a similar value ($k^0 = 2.1$ cm/s) was obtained by steady-state voltammetry for the reverse reaction. The pipettes were silanized and characterized by SECM and voltammetry. The fit between the theory and experimental curves was very good; however, the corresponding transfer coefficients, $\alpha = 0.70$ and $\beta = 0.60$, were larger than 0.5, and their sum was larger than the theoretically expected value of 1.0. Additionally, a noticeable inverse correlation between the k^0 and the a suggests that the data are not completely reliable. A slightly lower rate constant ($k^0 = 1.5 \pm 0.3$ cm/s) and $\alpha = 0.60 \pm 0.04$ were obtained for the tetramethylammonium transfer. One of the possible sources of error in these measurements was that the diffusion of the transferred ions inside the pipette was not taken into account.

Jing et al. studied IT kinetics at the nanoscopic water/*n*-octanol (OC) interface, which is often used as a model system to mimic CT processes through biomembranes.⁴¹ Although the potential window (~ 400 mV) was narrower than that observed with the same supporting electrolytes at the water/DCE interface, it was possible to obtain sufficiently well-defined steady-state voltammograms to determine partition coefficients and standard potentials for the transfers of tetraphenylarsonium, TBA^+ , and laurate from OC to water. These results suggest the possibility of a more straightforward approach to investigating the transfers of ionizable drugs through cell membranes. Kinetic parameters were determined for laurate transfer at the water/OC and water/DCE nanointerfaces, and the rate constant measured at the former was about six times slower.

Li et al.⁴² measured very large rate constants for simple transfers of TEA^+ (110 ± 23 cm/s) and ClO_4^- (35 ± 8 cm/s) and facilitated transfer of K^+ with DB18C6 (95 ± 31 cm/s) from extremely small ($1 \text{ nm} \leq a \leq 5 \text{ nm}$) water-filled pipettes to DCE. It was noticed later that the reported k^0 values may have been significantly overestimated because of problems with the data analysis and lack of pipette silanization.⁴³ Additional factors that could have increased the apparent IT rate constant are double-layer effects and possible deviations from the conventional theory at ultrasmall pipettes.

15.4.3.3 Some Experimental Issues

A number of experimental problems may plague kinetic experiments at the nano-ITIES. A hard question is whether the phase boundary is flat and located exactly at the pipette tip. In early studies at micrometer-sized pipettes, the assumption was that the water/organic interface is convex (i.e., protruding into the external liquid phase).⁵² In situ microscopy showed that a micropipette-supported ITIES tends to be flat when no external pressure is applied⁴⁹; however, a nanopipette tip is too small to be visualized by optical microscopy. The SECM approach curves obtained with nanopipette tips suggested that the ITIES is essentially flat and not recessed (see Section 15.3.2 and Chapter 18).

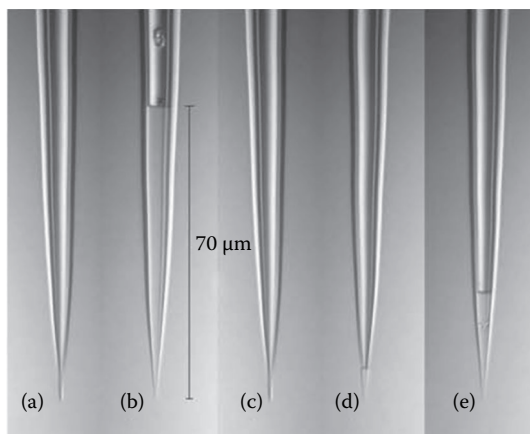


FIGURE 15.10 Sequential ingress/egress of water in a DCE-filled nanopipette. (a) Initial immersion, $E = +600$ mV; (b) ingress of water after the voltage was stepped to -100 mV and then to $+90$ mV; (c) complete egress of water at $E = +600$ mV; (d) same as (b) but with a shorter step time at $E = -100$ mV; (e) the voltage was stepped again to -100 mV and then back to $+90$ mV. The aperture radius was ~ 300 nm. The pipette was filled with 10 mM THATPBCl in DCE and immersed in 10 mM KF aqueous solution. (Adapted with permission Laforge, F.O., Carpino, J., Rotenberg, S. A., and Mirkin, M.V., Electrochemical attosyringe, *Proc. Natl. Acad. Sci. U.S.A.*, 2007, 104, 11895–11900. Copyright 2007 National Academy of Science, U.S.A.)

The shape and position of very small (e.g., < 5 nm) ITIES cannot be characterized at this time, and such interfaces are sometimes assumed to be essentially hemispherical.⁴²

It was also noticed that the outer organic solvent can get drawn inside a water-filled pipette and the thickness of the organic phase can vary with the voltage applied across the ITIES (Figure 15.10).^{56a} Similarly, one can fill a pipette with water and draw organic solution into it (and then eject it) by applying a suitable interfacial voltage. The movement of a micrometer-sized ITIES that accompanied IT was discussed in detail by Dale and Unwin.⁶⁹ The displacement of the liquid phase boundary during a voltammetric experiment can be a source of major distortions. In addition to changing the interfacial area, it may affect the mass-transfer rate and cause a significant increase in pipette resistance (if resistive organic solution is drawn inside the narrow shaft of the pipette). With no obvious way to detect or exclude the motion of a nano-ITIES, one has to assume that a well-shaped, sigmoidal, and retraceable voltammogram with a flat and stable diffusion limiting current is indicative of a stationary phase boundary.

Another source of uncertainty in defining the exact position of the ITIES is the glass roughness. This issue is especially important in the case of ultrasmall (e.g., $a \leq 5$ nm⁴²) pipettes, where even miniscule roughness of the glass surface should be comparable to the radius of the orifice. It was shown recently that the roughness of the pipette tip can be reduced by mechanical polishing^{48a} or by FIB milling.^{48b}

Kinetic analysis of nanopipette voltammograms can be further complicated by electrostatic effects produced by the negatively charged inner glass wall.^{43b} The surface charge can influence ion transport along the wall electrostatically and also affect the IT rate at the edge of the nano-ITIES. Various effects of the surface charge and electrical double layer present at the inner wall, including current rectification,⁷⁰ accumulation, or depletion of ions near the orifice⁷¹ and electrostatically gated transport⁷² have been reported for nanopipettes and glass nanopore electrodes immersed in an aqueous electrolyte solution (i.e., single-phase systems with no liquid/liquid interface).^{55a} In voltammetry across the nanoscale ITIES, the interfacial transfer of an ion at a few millimolars bulk concentration produces a pA-range current, which is much lower than that in single-phase experiments. Typically, the potential gradient and the ohmic potential drop inside the pipette are too small for significant electromigration or electro-osmotic flow along its charged inner wall.⁴³ The electrostatic

effects can be more important for smaller nanopipettes, for example, $a < 10$ nm, and more experiments are needed to check whether they can significantly influence kinetic parameters determined from IT voltammograms. Also, double-layer effects at the nanoscopic ITIES, where the diffusion layer thickness is comparable to that of the diffuse double layer, may result in deviations from the conventional electrochemical theory, as discussed for solid nanoelectrodes (see Chapter 2).

15.4.4 COMMON ION VOLTAMMETRY

A recently identified problem in the kinetic analysis of steady-state IT and ET voltammograms is the lack of the unique fit between the experimental and theoretical curves.

It was shown previously that a steady-state voltammogram is quasi-reversible when the dimensionless standard rate constant, $\lambda = k^0 a/D$, is ≤ 10 and kinetic parameters of interfacial CT reaction can, in principle, be extracted by fitting such a curve to the theory.^{20,59,60} However, this approach works well only if the shape of the voltammogram depends strongly on the values of kinetic parameters. For near-Nernstian CT processes (i.e., $1 \leq \lambda$), the same experimental voltammogram can be fit to the theory using different combinations of kinetic parameters with only minor adjustments in the formal potential value. For example, a satisfactory fit between experimental and theoretical voltammograms was obtained for IT of TEA⁺ at a nanopipette-supported ITIES with different k^0 (from 1.2 to 4.3 cm/s) and α (from 0.2 to 0.7) values.⁴³ The same problem can lead to large uncertainties in kinetic parameters extracted from near-Nernstian steady-state ET voltammograms.⁷³ It may have compromised the results of previously reported steady-state measurements of rapid ET kinetics at metal electrodes.

A simple modification was shown to essentially eliminate this problem and improve the accuracy and precision of CT kinetic measurements by steady-state voltammetry. For IT at the liquid/liquid interface, this approach—common ion voltammetry—is based on the addition of a transferable ion to both liquid phases, that is, the filling solution inside the pipette and the external solution.⁴³ The advantages of common ion voltammetry over the conventional protocol, in which a transferable ion is initially present only in one liquid phase, stem from the availability of two waves corresponding to the ingress of the common ion into the pipette and its egress to the external solution (positive and negative waves in Figure 15.11, respectively). If the D_1 and D_2 values are known, geometric parameters can be evaluated from the two limiting currents in the same voltammogram using Equations 15.7 and 15.8. Then, the unique combination of the kinetic parameters can be found by fitting an experimental voltammogram to the theory expressed by the following equation:^{43a}

$$\frac{i}{i_2} = \frac{1}{m_2/m_1 + m_2/k_b + k_f/k_b} \left(\frac{k_f}{k_b} - \frac{c_2^*}{c_1^*} \right) \quad (15.14)$$

where i_2 is the diffusion limiting current for ion ingress (Equation 15.7) shown in Figure 15.11; k_f and k_b are the heterogeneous rate constants given by the Butler–Volmer-type model; c_1 and c_2 are the bulk concentrations of the transferred ion in the outer and inner solutions, respectively; and $m_1 = (4f(\theta)D_1)/(\pi a)$ and $m_2 = (4xD_2)/(\pi a)$ are the mass-transfer coefficients representing ingress and egress transfers of the common ion.

The precision is further enhanced by directly determining the formal potential ($\Delta\phi^0$) from the potential of zero current (equilibrium potential, $\Delta\phi_{eq}$) given by the Nernst equation

$$\Delta\phi_{eq} = \Delta\phi^{0'} + \frac{RT}{zF} \ln \frac{c_2^*}{c_1^*} \quad (15.15)$$

instead of finding it from the fit of a conventional IT voltammogram to the theory.

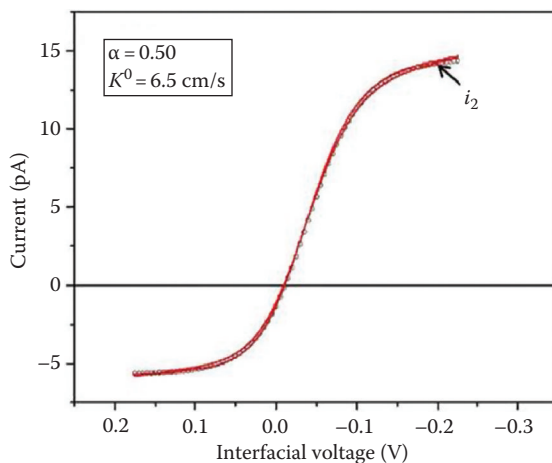


FIGURE 15.11 Steady-state common ion voltammogram of TEA^+ transfer across the DCE/water interface obtained with a 19 nm radius pipette (red curve). The best theoretical fit (symbols) to the experimental curve was calculated from Equation 15.14. The scan rate was 10 mV/s. (Reprinted with permission from Wang, Y., Velmurugan, J., Mirkin, M.V., Rodgers, P.J., Kim, J., and Amemiya, S., Kinetic study of rapid transfer of tetraethylammonium at the 1,2-dichloroethane/water interface by nanopipette voltammetry of common ion, *Anal. Chem.*, 2010, 82, 77–83. Copyright 2010 American Chemical Society.)

The unique fit of the experimental steady-state voltammogram to the theory can be obtained when both ingress and egress IT waves are quasi-reversible.⁴³ The asymmetry of the diffusion field results in different extents of reversibility (i.e., kinetic vs. diffusion control) of the ion ingress and egress processes, which can be assessed using two dimensionless parameters: $\lambda_1 = k^0/m_1$ and $\lambda_2 = k^0/m_2$. If the ratio of diffusion coefficients, D_2/D_1 , is not very far from the unity, reliable kinetic parameters can be extracted from a common ion voltammogram if both λ_{ing} and λ_{eg} are smaller than 10. In this way, the unique combination of the kinetic parameters, $\alpha = 0.50$ and $k^0 = 6.5$ cm/s, was obtained for the TEA^+ transfer across the water/DCE interface from the best fit shown in Figure 15.11.^{43b} Similar values ($k^0 = 6.1 \pm 0.9$ cm/s and $\alpha = 0.49 \pm 0.09$) were determined with various pipettes ($9.7 \text{ nm} \leq a \leq 33 \text{ nm}$) at different TEA^+ concentrations and essentially independent of a . These k^0 values are much higher than those determined previously from conventional nanopipette voltammograms⁴⁰ ($k^0 \sim 2$ cm/s). In the latter case, the analysis of a nearly reversible voltammogram with λ_{ing} (or λ_{eg}) > 1 did not give a unique combination of kinetic and thermodynamic parameters for rapid IT. An additional source of error was the neglected effect of ion diffusion in the internal solution.

Common ion voltammetry was employed to study IT reactions at the water/IL interface.⁴⁴ Kinetic measurements at such interfaces are challenging because of slow mass-transfer rates in IL. For instance, the IL employed in Ref. [44], $[\text{THTDP}^+][\text{C}_4\text{C}_4\text{N}^-]$, is ~ 700 times more viscous than water. Slow mass transfer in the IL phase results in a low diffusion current and at the same time necessitates the use of small nanopipettes and very low potential sweep rates to attain a steady state. Kinetic parameters of the TBA^+ transfer ($k^0 = 0.12 \pm 0.02$ cm/s and $\alpha = 0.50 \pm 0.06$) were extracted by fitting common ion voltammograms to the theory (Equation 15.14). Because of the large ratio of diffusion coefficients ($D_1/D_2 = 275$), the λ_2 values were much larger than the corresponding λ_1 values; and almost all λ_2 values were ≥ 10 . However, unlike water/organic interface, where $D_1/D_2 \approx 1$ and $\lambda_2 \geq 10$ corresponds to an essentially Nernstian IT, the ingress waves at the water/IL interface were quasi-reversible for $\lambda_2 \leq 50$. Several factors that could affect the results of kinetic experiments at the water/IL nanointerface were investigated. Very similar IT rate constants were determined for TBA^+ and similarly sized but asymmetric $\text{C}_8 \text{ mim}^+$ ion.

This result was taken as an evidence that ionic adsorption is not a major rate-determining factor in the studied system. The comparison of the diffusion currents produced by the egress of cations and anions from the water-filled nanopipettes ($a \geq 11$ nm) to IL showed that the mass transfer inside the pipette shaft is not significantly affected by migration and other electrostatic effects. No correlation was found between the interfacial size and IT kinetics, which would be indicative of double-layer effects.

A conceptually similar approach to measurements of rapid ET kinetics at nanoelectrodes requires both oxidized and reduced forms of redox species to be simultaneously present in solution.⁷³ An experimental voltammogram comprising steady-state oxidation and reduction waves can be used to determine mass-transfer coefficients of the reduced and oxidized form of electroactive species. The analysis of such curves should improve accuracy and precision of the evaluation of k^0 and α at nanoelectrodes.

15.5 SPECIAL NANO-ELECTROCHEMICAL PROBES

Several types of nanoelectrochemical probes surveyed in this section differ from those discussed earlier by their geometry and/or are designed for specific applications.

15.5.1 NANO-TLC

Nanometer-sized TLCs fabricated by several groups enabled electrochemical experiments in ultrasmall volumes, in which the total number of redox molecules could be varied between one and a few thousands. The pioneering studies conducted by the Bard group were aimed at observing single molecular events.³⁰ In those experiments, a Pt nanotip was recessed inside a small compartment formed within the wax insulator. A nano-TLC was produced by pushing such an electrode against a conducting surface. The redox cycling in such a cell is conceptually similar to the positive feedback in SECM: the redox mediator was oxidized (or reduced) at the nanoelectrode surface and regenerated via the reduction (or oxidation at the conductive substrate). With the TLC thickness sufficiently small (a few nanometers), the feedback process can provide sufficient amplification to measure the current produced by oxidation/reduction of a single redox molecule.³⁰ The voltammograms and current–time dependencies recorded in Ref. [30] exhibited high-amplitude current fluctuations, which were attributed to the migration of single electroactive molecules in and out of the TLC through a tiny hole in the wax insulator (for the discussion of single-molecule/single-nanoparticle electrochemistry, see Chapter 8).

In Ref. [33], nano-TLCs were prepared using recessed disk-type Pt electrodes ($a \geq 5$ nm; recess depth, ≥ 1 nm). A TLC was produced by immersing a recessed nanoelectrode in solution to fill its cavity and then transferring it into the pool of dry mercury. Because solution in this system was present only in the gap between Pt and Hg, there was no possibility of redox molecules escaping the cavity. Thus, unlike experiments described in Ref. [30], the recorded current did not exhibit significant fluctuations. The analysis of steady-state voltammograms yielded information about mass transfer, adsorption, ET kinetics, and double-layer effects on the nanoscale. The radius and the effective thickness of the TLC were determined from voltammetry and SECM. Although a good agreement was found between the determined TLC thickness and the recess depth of the nanoelectrode, more reliable characterization could probably be attained using the AFM (Section 15.2.3).

Several unusual size-related electrochemical phenomena were observed in nano-TLCs, including the current rectification due to nonpolarizability of the Hg electrode, strong dependence of the response on concentration of supporting electrolyte when the number of ionic species inside TLC becomes too small for the formation of two electrical double layers, and an enhanced voltammetric response to one redox species relative to the other.³³

Another approach to the preparation of nano-TLCs is to fabricate a nanogap device lithographically (see Chapter 16 for detailed discussion).⁶⁴ An advantage of this approach is in precise control

of the gap width and, therefore, high reproducibility of nanoelectrochemical experiments. A 50 nm thick nanofluidic cell with a well-defined geometry was used to measure kinetics of $\text{Fc}(\text{MeOH})_2$ oxidation with different supporting electrolytes.^{64a} While the kinetic parameters determined in KCl solutions were reasonably close to those measured by SECM for FcMeOH ,²⁰ the effects of the nature and concentration of electrolyte on k^0 and i_d values have yet to be clarified. All measurements in Ref. [64a] were made using essentially identical devices because, unlike SECM, neither the electrode radius nor the separation distance in the nano-TLC can be varied easily. A well-defined, smaller (30 nm thick) device was recently fabricated and used for amperometric detection of single molecules^{64b}; however, the thickness of lithographically prepared TLCs so far remains significantly larger than those attained using recessed nanoelectrodes.^{30,33} This resulted in a lower amplification level and small amplitude electrochemical signal (e.g., ~50 fA).

15.5.2 CARBON-BASED NANO-ELECTRODES AND PIPETTES

Different approaches to preparing carbon nanoelectrodes have been reported over the last decade.^{13,24b,27,74–76} Unlike metal microwires, carbon fibers cannot be easily pulled into glass capillaries, and the reported probes were often prepared by etching.^{13,74} Although etching can yield electrodes with extremely small effective radius (e.g., ~5 nm¹³), producing a carbon nanoprobe with a well-defined geometry is not straightforward.

Another approach is based on chemical vapor deposition (CVD) of carbon inside quartz nanopipettes,^{27,75–77} typically using methane or butane as a carbon source. The Bau and Gogotsi groups⁷⁵ developed detailed protocols for depositing different amounts of carbon on the inner pipette wall by varying a number of experimental parameters. The thickness and distribution of carbon layer depend on the CVD time, the composition of the gas mixture, the pipette shape, and tip diameter.^{75b} A relatively short CVD time resulted in the pipettes with an open path in the middle (Figure 15.12a). Conversely, by increasing CVD time and using a higher methane to argon ratio, one can increase the carbon layer thickness and close the path, leaving a cavity at the very end of tapered shaft (Figure 15.12b). Even longer deposition time (e.g., ~3 h) produced pipettes completely filled with carbon (Figure 15.12c).

Three types of carbon probes shown in Figure 15.12 have been employed in different experiments. Open carbon pipettes were inserted inside biological cells and used for concurrent intracellular injection and electrical measurements.⁷⁸ The pipettes in Ref. [78] had a relatively long (submicrometer to micron) piece of tapered carbon tube exposed to solution. Such a large conductive surface can be useful for potentiometric measurements, but not for amperometric experiments and applications requiring high z-axis resolution. A probe with the carbon layer confined to the inside of the quartz pipette (Figure 15.12a) is more suitable for amperometric applications and can be used as an SECM tip.⁷⁷ A possibility of using open carbon pipettes as rectification-based sensors and resistive-pulse sensors has been explored recently.⁷⁹

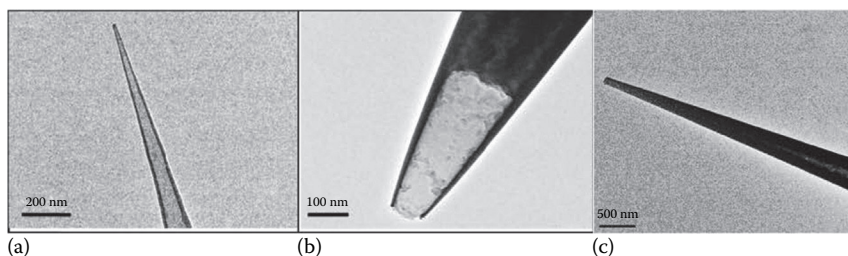


FIGURE 15.12 TEM images of carbon-coated nanopipettes. (a) An open pipette, $a=4$ nm, $\theta=2^\circ$; (b) a pipette with a nanocavity, $a=33$ nm, $\theta=8^\circ$, and the cavity depth equivalent to $\sim 12a$; and (c) a pipette completely filled with carbon, $a=50$ nm.

A carbon pipette with a nanocavity (Figure 15.12b) can be either prepared directly, as discussed earlier, or obtained by annealing a nanoelectrode for a few seconds in the oven to oxidize carbon in air.²⁷ The reported cavity depth was equivalent to ~4 to ~200 pipette radii depending on tip preparation conditions. The cavity can be filled with various solid or liquid agents to produce a sensor, for example, a nanosensor for reactive oxygen and nitrogen species was prepared by electrodepositing Pt black.²⁷ Such a probe can be used for amperometric and potentiometric measurements inside living cells. A carbon pipette with a nanocavity was also used for sampling attoliter-to-picoliter volumes of fluids and determining redox species by voltammetry and coulometry.⁷⁷ Very fast mass transport inside the carbon-coated nanocavity allows for rapid exhaustive electrolysis of the sampled material. The signal produced by oxidation/reduction inside the cavity can be significantly higher than the steady-state current to the orifice of the same pipette. The developed device is potentially useful for solution sampling from biological cells, micropores, and other microscopic objects.

An advantage of a flat carbon nanoelectrode (Figure 15.12c) over a wire-in-glass disk-type electrode with a similar radius of the conductive core is in a much smaller RG, which can be as small as that of a pulled quartz pipette (typically, <2). The resulting small physical size of the carbon probe is essential for intracellular measurements and high-resolution imaging. Thus, Takahashi et al.^{76a} used carbon tips to simultaneously obtain high-resolution topographical and electrochemical images of living cells. Actis et al.^{76b} showed that carbon nanoelectrodes can be inserted into individual cells both in tissue and in isolated cells to perform electrochemical measurements with minimal disruption to cell function. However, producing well-shaped, flat C nanoelectrodes is challenging. Polishing such electrodes is much harder than similarly sized metal nanoelectrodes (Section 15.2.1), and the utility of FIB milling has yet to be demonstrated. A very simple methodology for fabricating nanoelectrodes developed in Ref. [76] is based on the pyrolytic deposition of C from butane, which was passed through the quartz pipette by using a Tygon tube. The taper of the pipette was inserted into another quartz capillary, which was filled with N₂ to prevent oxidation of the carbon structure formed and bending of the capillary by high temperature. To form a pyrolytic carbon layer inside the capillary, the pipette taper was then heated with a Bunsen burner for a few seconds. Although very easy and efficient (takes ~1 min per electrode^{76b}), this method is not likely to yield electrodes with well-defined geometry, as can be seen from SECM approach curves presented in Ref. [76]. Multifunctional carbon nanoelectrodes with well-defined geometry were fabricated recently by CVD of parylene, followed by thermal pyrolysis and FIB milling.^{24b}

15.5.3 DUAL NANO-ELECTRODES AND PIPETTES

Electrochemical nanoprobe with two closely separated sensing elements have been fabricated and used either for generation/collection (G/C) experiments or for simultaneous recording of two different signals. Such a probe can consist of either two solid nanoelectrodes (e.g., two disk-type electrodes or a disk and a concentric ring)^{27b,80–83} or two liquid–liquid nanointerfaces⁸⁴ or a combination of a nanoelectrode and an open nanopipette.^{27b,85,86} Dual probes are produced either by using θ -tubing or by forming a concentric conducting ring surrounding a disk electrode. Most dual solid electrodes and nanoelectrode–nanopipette probes were used as tips in SECM or SICM; these publications are surveyed in Chapter 18. Dual pipettes (or θ -pipettes) were also employed in scanning probe experiments, including different versions of reactant delivery in SICM⁸⁷ and SECCM (Chapter 19).

Shao et al.⁸⁴ developed the θ -pipette-based G/C technique as a tool for studying heterogeneous IT reactions and homogeneous chemical reactions of ionic species in solution. They fabricated sub-micrometer- and nanometer-sized dual pipettes from borosilicate θ -tubing using a laser puller and formed two independent ITIES at the tip of such a device. Figure 15.13a illustrates the geometry, and Figure 15.13b shows an SEM image of a θ -shaped tip. Typically, both barrels of the dual pipette are filled with water.

If one of the barrels (*generator*) contains a cation, it can be transferred to the outer organic solvent by biasing this pipette at a sufficiently positive potential (E_g). A significant fraction of ejected

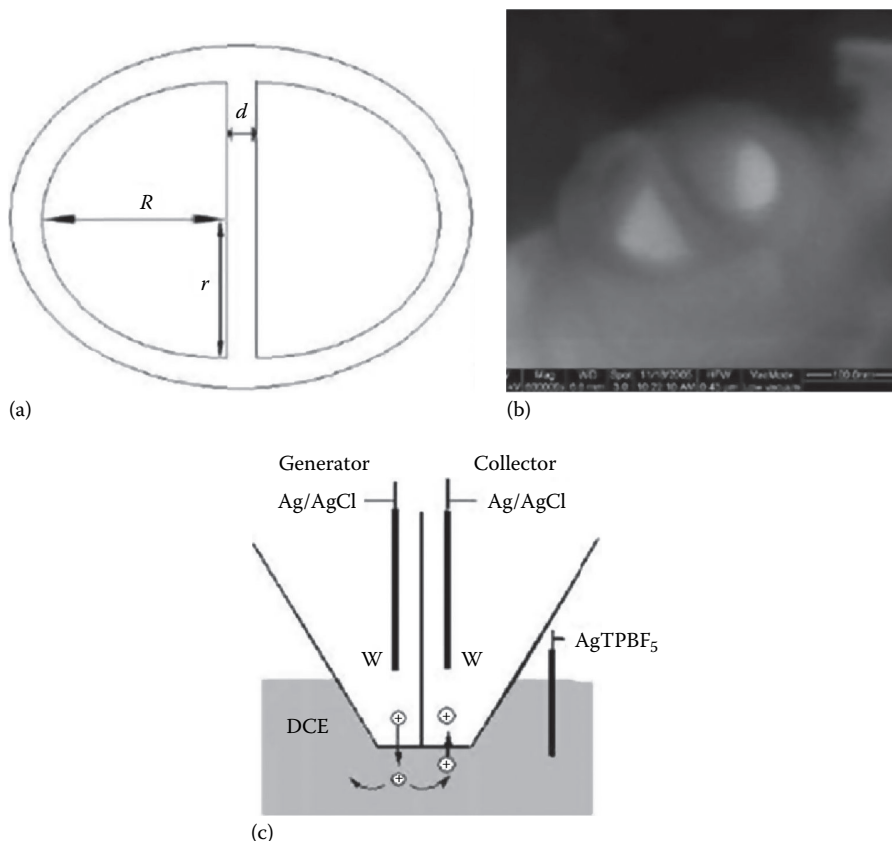


FIGURE 15.13 (a) Schematic representation of the θ -pipette, (b) an SEM image of the pipette with $R = 65$ nm and $d = 36$ nm, and (c) the G/C IT process at two liquid/liquid interfaces supported at the pipette tip. (Reprinted with permission from Hu, S., Xie, X., and Meng, P. et al., Fabrication and characterization of submicrometer- and nanometer-sized double-barrel pipettes, *Anal. Chem.*, 2006, 78, 7034–7039. Copyright 2006 American Chemical Society.)

cations reaches the negatively biased second pipette (*collector*) and gets transferred back into the aqueous phase (Figure 15.13c). The collection efficiency, $\eta = i_c/i_g$ (i_c is the collector current and i_g is the generator current), can be used to investigate CT and chemical reactions occurring in the space between two channels.⁸⁴ The η value depends on the collection potential and the geometry of the θ -pipette. In the absence of chemical reactions in solution, its maximum value, η_{\max} , is obtained when all ions reaching the opening of the collector pipette are transferred into it. The η_{\max} value depends only on the normalized distance between the centers of two barrels. The K^+ transfer at the W/DCE interface facilitated by DB18C6 was used as the model system to study the effects of geometric parameters of the pipette on collection efficiency. The larger, submicrometer-sized pipettes showed higher collection efficiency, while nanometer-sized pipettes produced better results for a system without supporting electrolyte.^{84d}

The dual-pipette technique allows quantitative separation of different IT and ET processes simultaneously occurring at the liquid/liquid interface (e.g., simple transfer of potassium, facilitated transfer of the same ion with a crown ether, and IT of supporting electrolyte). It can also be used to overcome potential window limitations and study numerous important reactions occurring at high positive or negative voltages applied across an ITIES (e.g., transfers of alkali metals from water to organic media).

15.5.4 ELECTROCHEMICAL ATTOSYRINGE

Laforge et al.^{56a} showed that a nanopipette can also be used as an *electrochemical attosyringe* for controlled fluid delivery. The prepared nanopipette was filled with an organic solvent and immersed in an aqueous solution. The ITIES at the pipette orifice was shown to move in response to variations in applied voltage. Water entered the pipette when the potential of the inner organic solution was made negative and was expelled at positive potentials (Figure 15.10). This phenomenon was used to sample and deliver attoliter-to-picoliter volumes of fluorescent dyes into human breast cells in culture. The injection volumes could be monitored and evaluated by measuring the pipette resistance and/or current vs. potential curves. Compared to other existing microinjectors, this device is inexpensive and easy to fabricate and use; it can be made very small and used repeatedly. Potential applications are in cell biology, nanolithography, and microfluidics.

Actis et al.⁸⁸ used an attosyringe as a scanning probe to sample small amounts of total RNA and mitochondrial DNA from a single cell. This approach, which the authors called *single-cell nanobiopsy*, offers the subcellular resolution and a minimal disruption of the cell function due to a small pipette size. The reported cellular survival rate was higher than 70%.

15.6 SUMMARY AND OUTLOOK

The use of nanometer-sized electrodes and liquid nanointerfaces enabled experimentalists to study a number of systems and processes that would not be accessible by macroscopic electrochemical probes. Some reported results, including incredibly fast rate constants of CT reactions,^{10b,42} multiple nucleation of metal on extremely small (~5 nm) electrodes,¹³ unusual transport phenomena,³⁵ and incompletely charged electrical double layer,³³ may be hard to reconcile with the existing theory. High spatial resolution of nanoelectrode experiments enables localized measurements of physicochemical properties that can challenge the consensus based on macroscopic electrochemical measurements.⁸⁹ In such extreme cases as well as in more routine kinetic experiments, the thorough characterization of nanoelectrodes and nanopipettes is essential to avoid misleading or highly inaccurate results. Unfortunately, the data obtained at nanoelectrodes characterized only by extracting the effective radius value from a steady-state voltammogram continue to be published. In addition to double-layer effects and other sources of deviations from conventional electrochemical theory discussed in Chapters 1 and 2, a number of experimental factors, such as the effects of the metal/insulator boundary and charged inner wall of a nanopipette on interfacial CT reactions, have to be better understood to ensure meaningful data analysis.

ACKNOWLEDGMENTS

Our research on nanoelectrochemistry has been supported by the National Science Foundation (CHE-1026582, CHE-1300158, and CBET-1251232) and AFOSR MURI (FA9550-14-1-0003).

REFERENCES

1. (a) Murray, R. W. 2008. Nanoelectrochemistry: Metal nanoparticles, nanoelectrodes, and nanopores. *Chem. Rev.* 108:2688–2720. (b) Oja, S. M., Wood, M., and Zhang, B. 2013. Nanoscale electrochemistry. *Anal. Chem.* 85:473–486. (c) Chen, S. and Liu, Y. 2014. Electrochemistry at nanometer-sized electrodes. *Phys. Chem. Chem. Phys.* 16:635–652.
2. (a) Wehmeyer, K. R., Deakin, M. R., and Wightman, R. M. 1985. Electroanalytical properties of band electrodes of submicrometer width. *Anal. Chem.* 57:1913–1916. (b) Bond, A. M. 1986. Theory and experimental characterization of linear gold microelectrodes with submicrometer thickness. *J. Phys. Chem.* 90:2911–2917. (c) Morris, R., Franta, D. J., and White, H. S. 1987. Electrochemistry at platinum bane electrodes of width approaching molecular dimensions: Breakdown of transport equations at very small electrodes. *J. Phys. Chem.* 91:3559–3564.

3. Shao, Y. and Mirkin, M. V. 1997. Fast kinetic measurements with nanometer-sized pipettes. Transfer of potassium ion from water into dichloroethane facilitated by dibenzo-18-crown-6. *J. Am. Chem. Soc.* 119:8103–8104.
4. (a) Arrigan, D. W. M. 2004. Nanoelectrodes, nanoelectrode arrays and their applications. *Analyst* 129:1157–1165. (b) Cox, J. T. and Zhang, B. 2012. Nanoelectrodes: Recent advances and new directions. *Annu. Rev. Anal. Chem.* 5:253–272.
5. Shen, M., Ishimatsu, R., Kim, J., and Amemiya, S. 2012. Quantitative imaging of ion transport through single nanopores by high-resolution scanning electrochemical microscopy. *J. Am. Chem. Soc.* 134:9856–9859.
6. Li, Y., Cox, J. T., and Zhang, B. 2010. Electrochemical response and electrocatalysis at single Au nanoparticles. *J. Am. Chem. Soc.* 132:3047–3054.
7. Velmurugan, J., Noël, J.-M., Nogala, W., and Mirkin, M. V. 2012. Nucleation and growth of metal on nanoelectrodes. *Chem. Sci.* 3:3307–3314.
8. Gewirth, A. A., Craston, D. H., and Bard, A. J. 1989. Fabrication and characterization of microtips for in situ scanning tunneling microscopy. *J. Electroanal. Chem.* 261:477–482.
9. Nagahara, L. A., Thundat, T., and Lindsay, S. M. 1989. Preparation and characterization of STM Tips for electrochemical studies. *Rev. Sci. Instrum.* 60:3128–3130.
10. (a) Penner, R. M., Heben, M. J., and Lewis, N. S. 1989. Preparation and electrochemical characterization of conical and hemispherical ultramicroelectrodes. *Anal. Chem.* 61:1630–1636. (b) Penner, R. M., Heben, M. J., Longin, T. L., and Lewis, N. S. 1990. Fabrication and use of nanometer-sized electrodes in electrochemistry. *Science* 250:1118–1121.
11. Sun, P., Zhang, Z., Guo, J., and Shao, Y. 2001. Fabrication of nanometer-sized electrodes and tips for scanning electrochemical microscopy. *Anal. Chem.* 73:5346–5351.
12. Slevin, C. J., Gray, N. J., Macpherson, J. V., Webb, M. A., and Unwin, P. R. 1999. Fabrication and characterisation of nanometre-sized platinum electrodes for voltammetric analysis and imaging. *Electrochem. Commun.* 1:282–288.
13. Chen, S. L. and Kucernak, A. 2002. Fabrication of carbon microelectrodes with an effective radius of 1 nm. *Electrochem. Commun.* 4:80–85.
14. (a) Mirkin, M. V., Fan, F.-R. F., and Bard, A. J. 1992. Scanning electrochemical microscopy. 13. Evaluation of the tip shapes of nanometer size microelectrodes. *J. Electroanal. Chem.* 328:47–62. (b) Mirkin, M. V., Fan, F.-R. F., and Bard, A. J. 1992. Direct electrochemical measurements inside a 2000 Å—Thick polymer film by scanning electrochemical microscopy. *Science* 257:364–366.
15. Watkins, J. J., Chen, J. Y., White, H. S., Abruna, H. D., Maisonhaute, E., and Amatore, C. 2003. Zeptomole voltammetric detection and electron-transfer rate measurements using platinum electrodes of nanometer dimensions. *Anal. Chem.* 75:3962–3971.
16. (a) Hills, G. J., Schiffrin, D. J., and Thompson, J. 1974. Electrochemical nucleation from molten salts. Part I: Diffusion controlled electrodeposition of silver from alkali molten nitrates. *Electrochim. Acta* 19:657–670. (b) Branco, P. D., Mostany, J., Borrás, C., and Scharifker, B. R. 2009. The current transient for nucleation and diffusion-controlled growth of spherical caps. *J. Solid State Electrochem.* 13:565–571.
17. (a) Wehmeyer, K. R. and Wightman, R. M. 1985. Cyclic voltammetry and anodic stripping voltammetry with mercury ultra-microelectrodes. *Anal. Chem.* 57:1989–1993. (b) Velmurugan, J. and Mirkin, M. V. 2010. Fabrication of nanoelectrodes and metal clusters by electrodeposition. *ChemPhysChem* 11: 3011–3017. (c) Mauzeroll, J., Hueske, E. A., and Bard, A. J. 2003. Scanning electrochemical microscopy. 48. Hg/Pt hemispherical ultramicroelectrodes: Fabrication and characterization. *Anal. Chem.* 75:3880–3889.
18. Shao, Y., Mirkin, M. V., Fish, G., Kokotov, S., Palanker, D., and Lewis, A. 1997. Nanometer-sized electrochemical sensors. *Anal. Chem.* 69:1627–1634.
19. Zhang, B., Galusha, J., Shiozawa, P. G., Wang, G. L., Bergren, A. J., Jones, R. M., White, R. J., Ervin, E. N., Cauley, C. C., and White, H. S. 2007. Bench-top method for fabricating glass-sealed nanodisk electrodes, glass nanopore electrodes, and glass nanopore membranes of controlled size. *Anal. Chem.* 79:4778–4787.
20. Sun, P. and Mirkin, M. V. 2006. Kinetics of electron transfer reactions at nanoelectrodes. *Anal. Chem.* 78:6526–6534.
21. (a) Velmurugan, J., Sun, P., and Mirkin, M. V. 2009. Scanning electrochemical microscopy with gold nanotips: The effect of electrode material on electron transfer rates. *J. Phys. Chem. C* 113:459–464. (b) Noël, J.-M., Velmurugan, J., Gökmeşe, E., and Mirkin, M. V. 2013. Fabrication, characterization and chemical etching of Ag nanoelectrodes. *J. Solid State Electrochem.* 17:385–389.

22. Li, Y., Bergman, D. and Zhang, B. 2009. Preparation and electrochemical response of 1–3 nm Pt disk electrodes. *Anal. Chem.* 81:5496–5502.
23. (a) Katemann, B. B. and Schuhmann, W. 2002. Fabrication and characterization of needle-type Pt-disk nanoelectrodes. *Electroanalysis* 14:22–28. (b) Mezour, M. A., Morin, M., and Mauzeroll, J. 2011. Fabrication and characterization of laser pulled platinum microelectrodes with controlled geometry. *Anal. Chem.* 83:2378–2382.
24. (a) Nioradze, N., Chen, R., Kim, J., Shen, M., Santhosh, P., and Amemiya, S. 2013. Origins of nanoscale damage to glass-sealed platinum electrodes with submicrometer and nanometer size. *Anal. Chem.* 85:6198–6202. (b) Thakar, R., Weber, A. E., Morris, C. A., Baker, L. A. 2013. Multifunctional carbon nanoelectrodes fabricated by focused ion beam milling. *Analyst* 138:5973–5982.
25. Jena, B. K., Percival, S. J., and Zhang, B. 2010. Au disk nanoelectrode by electrochemical deposition in a nanopore. *Anal. Chem.* 82:6737–6743.
26. Wang, Y., Noel, J.-M., Velmurugan, J., Nogala, W., Mirkin, M. V., Lu, C., Guille Collignon, M., Lemaître, F., and Amatore, C. 2012. Nanoelectrodes for determination of reactive oxygen and nitrogen species inside murine macrophages. *Proc. Natl. Acad. Sci. U. S. A.* 109:11534–11539.
27. Hu, K., Gao, Y., Wang, Y. et al. 2013. Platinized carbon nanoelectrodes as potentiometric and amperometric SECM probes. *J. Solid State Electrochem.* 17:2971–2977.
28. (a) Baranski, A. S. 1991. On possible systematic errors in determinations of charge transfer kinetics at very small electrodes. *J. Electroanal. Chem.* 307:287–292. (b) Oldham, K. B. 1992. A hole can serve as a microelectrode. *Anal. Chem.* 64:646–651.
29. Nogala, W., Velmurugan, J., and Mirkin, M. V. 2012. Atomic force microscopy of electrochemical nanoelectrodes. *Anal. Chem.* 84:5192–5197.
30. (a) Fan, F.-R. F. and Bard, A. J. 1995. Electrochemical detection of single molecules. *Science* 267:871–874. (b) Fan, F. R. F., Kwak, J., and Bard, A. J. 1996. Single molecule electrochemistry. *J. Am. Chem. Soc.* 118:9669–9675.
31. Sun, P. and Mirkin, M. V. 2007. Scanning electrochemical microscopy with slightly recessed nanotips. *Anal. Chem.* 79:5809–5816.
32. (a) Zhang, B., Zhang, Y. H., and White, H. S. 2004. The nanopore electrode. *Anal. Chem.* 76:6229–6238. (b) Zhang, B., Zhang, Y. H., and White, H. S. 2006. Steady-state voltammetric response of the nanopore electrode. *Anal. Chem.* 78:477–483. (c) Sun, P. 2010. Cylindrical nanopore electrode and its application to the study of electrochemical reaction in several hundred attoliter volume. *Anal. Chem.* 82:276–281.
33. Sun, P. and Mirkin, M. V. 2008. Electrochemistry of individual molecules in zeptoliter volumes. *J. Am. Chem. Soc.* 130:8241–8250.
34. (a) Bond, A. M., Oldham, K. B., and Zoski, C. G. 1989. Steady-state voltammetry. *Anal. Chim. Acta* 216:177–230. (b) Wightman, R. M. and Wipf, D. O. 1989. Voltammetry at ultramicroelectrodes. In *Electroanalytical Chemistry*, vol. 15, Bard, A. J. (ed.), pp. 267–353. New York: Marcel Dekker. (c) Amatore, C. 1995. Electrochemistry at ultramicroelectrodes. In *Physical Electrochemistry: Principles, Methods, and Applications*, Rubinstein, I. (ed.), pp. 131–208. New York: Marcel Dekker.
35. Sun, Y., Liu, Y., Liang, Z., Xiong, L., Wang, A., and Chen, S. 2009. On the applicability of conventional voltammetric theory to nanoscale electrochemical interfaces. *J. Phys. Chem. C* 113:9878–9883.
36. Zhang, Y., Zhou, J., Lin, L., and Lin, Z. 2008. Determination of electrochemical electron-transfer reaction standard rate constants at nanoelectrodes: Standard rate constants for ferrocenylmethyltrimethylammonium(III)/(II) and hexacyanoferrate(III)/(II). *Electroanalysis* 20:1490–1494.
37. Noël, J.-M., Yu, Y., and Mirkin, M. V. 2013. Dissolution of Pt at moderately negative potentials during oxygen reduction in water and organic media. *Langmuir* 29:1346–1350.
38. Taylor, G. and Girault, H. H. 1986. Ion transfer reactions across a liquid–liquid interface supported on a micropipette tip. *J. Electroanal. Chem.* 208:179–183.
39. Amemiya, S., Wang, Y., and Mirkin, M. V. 2013. Nanoelectrochemistry at the liquid/liquid interfaces. In *Specialist Periodical Reports in Electrochemistry*, vol. 12, Compton, R. and Wadhawan, J. (eds.), pp. 1–43. RSC Publishing.
40. Cai, C. X., Tong, Y. H., and Mirkin, M. V. 2004. Probing rapid ion transfer across nanoscopic liquid–liquid interface. *J. Phys. Chem. B* 108:17872–17878.
41. Jing, P., Zhang, M. Q., Hu, H., Xu, X. D., Liang, Z. W., Li, B., Shen, L., Xie, S. B., Pereira, C. M., and Shao, Y. H. 2006. Ion-transfer reactions at the nanoscopic water/n-octanol interface. *Angew. Chem. Int. Ed.* 45:6861–6864.
42. Li, Q., Xie, S., Liang, Z., Meng, X., Liu, S., Girault, H. H., and Shao, Y. 2009. Fast ion-transfer processes at nanoscopic liquid/liquid interfaces. *Angew. Chem. Int. Ed.* 48:8010–8013.

43. (a) Rodgers, P. J., Amemiya, S., Wang, Y., and Mirkin, M. V. 2010. Nanopipette voltammetry of common ion across a liquid–liquid interface. Theory and limitations in kinetic analysis of nanoelectrode voltammograms. *Anal. Chem.* 82:84–90. (b) Wang, Y., Velmurugan, J., Mirkin, M. V., Rodgers, P. J., Kim, J., and Amemiya, S. 2010. Kinetic study of rapid transfer of tetraethylammonium at the 1,2-dichloroethane/water interface by nanopipette voltammetry of common ion. *Anal. Chem.* 82:77–83.
44. Wang, Y., Kakiuchi, T., Yasui, Y., and Mirkin, M. V. 2010. Kinetics of ion transfer at the ionic liquid/water nanointerface. *J. Am. Chem. Soc.* 132:16945–16952.
45. Yuan, Y. and Shao, Y. H. 2002. Systematic investigation of alkali metal ion transfer across the micro- and nano-water/1,2-dichloroethane interfaces facilitated by dibenzo-18-crown-6. *J. Phys. Chem. B* 106:7809–7814.
46. Cai, C. and Mirkin, M. V. 2006. Electron transfer kinetics at polarized nanoscopic liquid/liquid interfaces. *J. Am. Chem. Soc.* 128:171–179.
47. Brown, K. T. and Flaming, D. G. 1986. *Advanced Micropipette Techniques for Cell Physiology*. New York: Wiley.
48. (a) Elsamadisi, P., Wang, Y., Velmurugan, J., and Mirkin, M. V. 2011. Polished nanopipets: New probes for high-resolution scanning electrochemical microscopy. *Anal. Chem.* 83:671–673. (b) Kim, J., Izadyar, A., Shen, M., Ishimatsu, R., and Amemiya, S. 2014. Ion Permeability of the nuclear pore complex and ion-induced macromolecular permeation as studied by scanning electrochemical and fluorescence microscopy. *Anal. Chem.* 86:2090–2098.
49. Shao, Y. and Mirkin, M. V. 1998. Voltammetry at micropipette electrodes. *Anal. Chem.* 70:3155–3161.
50. Laforge, F. O., Velmurugan, J., Wang, Y., and Mirkin, M. V. 2009. Nanoscale imaging of surface topography and reactivity with the scanning electrochemical microscope (SECM). *Anal. Chem.* 81:3143–3150.
51. Kim, J., Shen, M., Nioradze, N., and Amemiya, S. 2012. Stabilizing nanometer scale tip-to-substrate gaps in scanning electrochemical microscopy using an isothermal chamber for thermal drift suppression. *Anal. Chem.* 84:3489–3492.
52. Beattie, P. D., Delay, A., and Girault, H. H. 1995. Investigation of the kinetics of assisted potassium ion transfer by dibenzo-18-crown-6 at the micro-ITIES by means of steady-state voltammetry. *J. Electroanal. Chem.* 380:167–175.
53. (a) Shoup, D. and Szabo, A. 1984. Influence of insulation geometry on the current at microdisk electrodes. *J. Electroanal. Chem.* 160:27–31. (b) Zoski, C. G. and Mirkin, M. V. 2002. Steady-state limiting currents at finite conical microelectrodes. *Anal. Chem.* 74:1986–1992.
54. Rodgers, P. J. and Amemiya, S. 2007. Cyclic voltammetry at micropipette electrodes for the study of ion-transfer kinetics at liquid/liquid interfaces. *Anal. Chem.* 79:9276–9285.
55. (a) Morris, C., Friedman, A. K., and Baker, L. A. 2010. Applications of nanopipettes in the analytical sciences. *Analyst* 135:2190–2202. (b) Chen, C.-C., Zhou, Y., and Baker, L. A. 2012. Scanning ion conductance microscopy. *Annu. Rev. Anal. Chem.* 5:207–228.
56. (a) Laforge, F. O., Carpino, J., Rotenberg, S. A., and Mirkin, M. V. 2007. Electrochemical Attosyringe. *Proc. Natl. Acad. Sci. USA* 104:11895–11900. (b) Wang, Y., Kececi, K., Mirkin, M. V., Mani, V., Sardesai, N., and Rusling, J. F. 2013. Quantitative resistive-pulse measurements with nanopipettes: Detection of Au nanoparticles and nanoparticle-bound anti-peanut IgY. *Chem. Sci.* 4:655–663.
57. (a) Tsujioka, N., Imakura, S., Nishi, N., and Kakiuchi, T. 2006. Voltammetry of ion transfer across the electrochemically polarized micro liquid-liquid interface between water and a room-temperature ionic liquid, tetrahexylammonium bis(trifluoromethylsulfonyl)imide, using a glass capillary micropipette. *Anal. Sci.* 22:667–671. (b) Nishi, N., Imakura, S., and Kakiuchi, T. 2008. A digital simulation study of steady-state voltammograms for the ion transfer across the liquid–liquid interface formed at the orifice of a micropipette. *J. Electroanal. Chem.* 621:297–303.
58. Bard, A. J. and L. R. Faulkner. 2001. *Electrochemical Methods: Fundamentals and Applications*, 2nd edn. New York: John Wiley & Sons.
59. Oldham, K. B. and Zoski, C. G. 1988. Comparison of voltammetric steady states at hemispherical and disc microelectrodes. *J. Electroanal. Chem.* 256:11–19.
60. Mirkin, M. V. and Bard, A. J. 1992. A simple analysis of quasi-reversible steady-state voltammograms. *Anal. Chem.* 64:2293–2202.
61. Stewart, A. A., Taylor, G., Girault, H. H., and McAleer, J. 1990. Voltammetry at micro ITIES supported at the tip of a micropipette: Part I. Linear sweep voltammetry. *J. Electroanal. Chem.* 296:491–515.
62. Watkins, J. J. and White, H. S. 2004. The role of the electrical double layer and ion pairing on the electrochemical oxidation of hexachloroiridate(III) at Pt electrodes of nanometer dimensions. *Langmuir* 20:5474–5483.

63. (a) Smith, C. P. and White, H. S. 1993. Theory of the voltammetric response of electrodes of submicron dimensions. Violation of electroneutrality in the presence of excess supporting electrolyte. *Anal. Chem.* 65:3343–3353. (b) He, R., Chen, S., Yang, F., and Wu, B. 2006. Dynamic diffuse double-layer model for the electrochemistry of nanometer-sized electrodes. *J. Phys. Chem. B* 110:3262–3270. (c) Liu, Y., He, R., Zhang, Q., and Chen, S. 2010. Theory of electrochemistry at nanometer-sized disk electrodes. *J. Phys. Chem. C* 114:10812–10822.
64. (a) Zevenbergen, M. A. G., Wolfrum, B. L., Goluch, E. D., Singh, P. S., and Lemay, S. G. 2009. Fast electron-transfer kinetics probed in nanofluidic channels. *J. Am. Chem. Soc.* 131:11471–11477. (b) Zevenbergen, M. A. G., Singh, P. S., Goluch, E. D., Wolfrum, B. L., and Lemay, S. G. 2011. Stochastic sensing of single molecules in a nanofluidic electrochemical device. *Nano Lett.* 11, 2881–2886.
65. (a) Amemiya, S., Nioradze, N., Santhosh, P., and Deible, M. J. 2011. Generalized theory for nanoscale voltammetric measurements of heterogeneous electron-transfer kinetics at macroscopic substrates by scanning electrochemical microscopy. *Anal. Chem.* 83:5928–5935. (b) Nioradze, N., Kim, J., and Amemiya, S. 2011. Quasi-steady-state voltammetry of rapid electron transfer reactions at the macroscopic substrate of the scanning electrochemical microscope. *Anal. Chem.* 83:828–835.
66. Garcia-Morales, V. and Krischer, K. 2010. Fluctuation enhanced electrochemical reaction rates at the nanoscale. *Proc. Natl. Acad. Sci. U. S. A.* 107:4528–4532.
67. Geblewicz, G. and Schiffrin, D. J. 1988. Electron transfer between immiscible solutions: The hexacyanoferrate-lutetium biphthalocyanine. *J. Electroanal. Chem.* 244:27–37.
68. Zhan, D. P., Yuan, Y., Xiao, Y. J., Wu, B. L., and Shao, Y. H. 2002. Alkali metal ions transfer across a water/1,2-dichloroethane interface facilitated by a novel monoaza-B15C5 derivative. *Electrochim. Acta* 47:4477–4483.
69. Dale, S. E. C. and Unwin, P. R. 2008. Polarised liquid/liquid micro-interfaces move during charge transfer. *Electrochem. Commun.* 10:723–726.
70. Wei, C., Bard, A. J., and Feldberg, S. W. 1997. Current rectification at quartz nanopipet electrodes. *Anal. Chem.* 69:4627–4633.
71. (a) White, H. S. and Bund, A. 2008. Ion current rectification at nanopores in glass membranes. *Langmuir* 24:2212–2218. (b) Calander, N. 2009. Analyte concentration at the tip of a nanopipette. *Anal. Chem.* 81:8347–8353.
72. Wang, G., Zhang, B., Wayment, J. R., Harris, J. M., and White, H. S. 2006. Electrostatic-gated transport in chemically modified glass nanopore electrodes. *J. Am. Chem. Soc.* 128:7679–7686.
73. Yu, Y., Velmurugan, J., and Mirkin, M. V., unpublished results.
74. Huang, W. H., Pang, D. W., Tong, H., Wang, Z. L., Cheng, J. K. 2001. A method for the fabrication of low-noise carbon fiber nanoelectrodes. *Anal. Chem.* 73:1048–1052.
75. (a) Kim, B. M., Murray, T., and Bau, H. H. 2005. The fabrication of integrated carbon pipes with sub-micron diameters. *Nanotechnology* 16:1317–1320. (b) Vitol, E.; Schrlau, M. G., Bhattacharyya, S., Ducheyne, P., Bau, H. H., Friedman, G., Gogotsi, Y. 2009. Effects of deposition conditions on the structure and chemical properties of carbon nanopipettes. *Chem. Vap. Deposit.* 15:204–208. (c) Singhal, R., Bhattacharyya, S., Orynbayeva, Z., Vitol, E., Friedman, G., and Gogotsi, Y. 2010. Small diameter carbon nanopipettes. *Nanotechnology* 21:015304.
76. (a) Takahashi, Y., Shevchuk, A. I., Novak, P. et al. 2012. Topographical and electrochemical nanoscale imaging of living cells using voltage-switching mode scanning electrochemical microscopy. *Proc. Natl. Acad. Sci. U. S. A.* 109:11540–11545. (b) Actis, P., Tokar, S., Clausmeyer, J. et al. 2014. Electrochemical nanopores for single-cell analysis. *ACS Nano* 8:875–884. DOI: 10.1021/nn405612q.
77. Yu, Y., Noël, J.-M., Mirkin, M. V., Gao, Y., Mashtalir, O., Friedman, G., and Gogotsi, Y. 2014. Carbon pipette-based electrochemical nanosampler. *Anal. Chem.* 86:3365–3372.
78. Schrlau, M., Dun, N., and Bau, H. 2009. Cell electrophysiology with carbon nanopipettes. *ACS Nano* 3:563–568.
79. Hu, K., Wang, Y., Cai, H., Mirkin, M. V., Gao, Y., Fridman, G., and Gogotsi, Y. 2014. Open carbon nanopipettes as resistive-pulse sensors, rectification sensors and electrochemical nanopores. *Anal. Chem.* 86:8897–8901.
80. Yasukawa, T., Kaya, T., and Matsue, T. 1999. Dual imaging of topography and photosynthetic activity of a single protoplast by scanning electrochemical microscopy. *Anal. Chem.* 71:4637–4641.
81. Yang, C. and Sun, P. 2009. Fabrication and characterization of a dual submicrometer-sized electrode. *Anal. Chem.* 81:7496–7500.
82. McKelvey, K., Nadappuram, B. P., Actis, P. et al. 2013. Fabrication, characterization, and functionalization of dual carbon electrodes as probes for scanning electrochemical microscopy (SECM). *Anal. Chem.* 85:7519–7526.

83. Johnson, L. and Walsh, D. A. 2012. Tip generation–substrate collection–tip collection mode scanning electrochemical microscopy of oxygen reduction electrocatalysts. *J. Electroanal. Chem.* 682:45–52.
84. (a) Shao, Y., Liu, B., and Mirkin, M. V. 1998. Studying ionic reactions by new generation/collection technique. *J. Am. Chem. Soc.* 120:12700–12701. (b) Liu, B., Shao, Y., and Mirkin, M. V. 2000. Dual-pipette techniques for probing ionic reactions. *Anal. Chem.* 72:510–519. (c) Chen, Y., Gao, Z., Li, F. et al. 2003. Studies of electron-transfer and charge-transfer coupling processes at a liquid/liquid interface by double-barrel micropipette technique. *Anal. Chem.* 75:6593–6601. (d) Hu, S., Xie, X., Meng, P. et al. 2006. Fabrication and characterization of submicrometer- and nanometer-sized double-barrel pipettes. *Anal. Chem.* 78:7034–7039.
85. Takahashi, Y., Shevchuk, A. I., Novak, P. et al. 2011. Multifunctional nanoprobe for nanoscale chemical imaging and localized chemical delivery at surfaces and interfaces. *Angew. Chem. Int. Ed.* 50:9638–9642.
86. (a) Comstock, D. J., Elam, J. W., Pellin, M. J., and Hersam, M. C. 2010. Integrated ultramicroelectrode-nanopipet probe for concurrent scanning electrochemical microscopy and scanning ion conductance microscopy. *Anal. Chem.* 82:1270–1276. (b) Takahashi, Y., Shevchuk, A. I., Novak, P. et al. 2010. Simultaneous noncontact topography and electrochemical imaging by SECM/SICM featuring ion current feedback regulation. *J. Am. Chem. Soc.* 132:10118–10126.
87. (a) Rodolfa, K. T., Bruckbauer, A., Zhou, D., Korchev, Y. E., and Klennerman, D. 2005. Two-component graded deposition of biomolecules with a double-barreled nanopipette. *Angew. Chem., Int. Ed.* 44: 6854–6859. (b) Rodolfa, K. T., Bruckbauer, A., Zhou, D., Shevchuk, A. I., Korchev, Y. E., and Klennerman, D. 2006. Nanoscale pipetting for controlled chemistry in small arrayed water droplets using a double-barrel pipette. *Nano Lett.* 6:252–257.
88. Actis, P., Maalouf, M. M., Kim, H. J. et al. 2014. Compartmental genomics in living cells revealed by single-cell nanobiopsy. *ACS Nano* 8:546–553. DOI: 10.1021/nn405097u.
89. (a) Williams, C. G., Edwards, M. A., Colley, A. L., Macpherson, J. V., and Unwin, P. R. 2009. Scanning micropipette contact method for high-resolution imaging of electrode surface redox activity. *Anal. Chem.* 81:2486–2495. (b) Patel, A. N., Guille Collignon, M., O’Connell, M. A. et al. 2012. A new view of electrochemistry at highly oriented pyrolytic graphite. *J. Am. Chem. Soc.* 134:20117–20130.